nature communications

Article

https://doi.org/10.1038/s41467-024-49426-3

Definitive engineering strength and fracture toughness of graphene through on-chip nanomechanics

Received: 10 June 2023

Accepted: 25 April 2024

Published online: 12 July 2024

Check for updates

Sahar Jaddi[1] ✉, M. Wasil Malik[2,7], Bin Wang[2,3], Nicola M. Pugno[4,5], Yun Zeng[3], Michael Coulombier[1], Jean-Pierre Raskin[2] & Thomas Pardoen[1,6]

Fail-safe design of devices requires robust integrity assessment procedures which are still absent for 2D materials, hence affecting transfer to applications. Here, a combined on-chip tension and cracking method, and associated data reduction scheme have been developed to determine the fracture toughness and strength of monolayer-monodomain-freestanding graphene. Myriads of specimens are generated providing statistical data. The crack arrest tests provide a definitive fracture toughness of 4.4 MPa$\sqrt{m}$. Tension on-chip provides Young's modulus of 950 GPa, fracture strain of 11%, and tensile strength up to 110 GPa, reaching a record of stored elastic energy ~6 GJ m^{-3} as confirmed by thermodynamics and quantized fracture mechanics. A ~ 1.4 nm crack size is often found responsible for graphene failure, connected to 5-7 pair defects. Micron-sized graphene membranes and smaller can be produced defect-free, and design rules can be based on 110 GPa strength. For larger areas, a fail-safe design should be based on a maximum 57 GPa strength.

2D materials such as graphene have received attention in the context of a variety of potential applications driven by their exceptional properties[1]. Generally, 2D materials have a combined functional–structural role. However, the establishment of robust procedures that guarantee fail-safe designs for long-term reliable operation is essentially missing in the world of 2D materials. There is no doubt that the extreme strength (>100 GPa) and excellent ductility (>20%) predicted theoretically[2–4] and verified experimentally[5,6] on nanoscale specimens is a major asset. Nevertheless, literature studies are essentially limited to extremely small specimens, with limited statistical significance in terms of defect distribution and the number of test samples. In real applications involving wide 2D materials with a single or few layers, the failure resistance is dictated more by the population of defects than by the intrinsic strength and ductility. The literature mainly focuses on the fundamental mechanisms controlling the strength variations when contrasting defective and perfect lattice structures[7–12]. The context is exactly similar to brittle-type materials with covalent or ionic bonds, such as for silicon with a theoretical strength of >25 GPa and fracture strain >20%[13] that, at the macroscopic wafer level, drops down to ~300 MPa and ~0.2%, respectively[14]. Reconciliation between theoretical and in-use values comes through fracture mechanics theory assuming a population of crack-type defects and Weibull analysis[15]. However, this approach requires generating reliable fracture toughness data with statistical value and the determination of the nature of the defects. This leads to major challenges in the context of 2D materials such as graphene.

Several approaches have been proposed to determine the mechanical properties of 2D materials. Deflection of suspended graphene membranes has generally been performed using an atomic force microscope tip[6], which, when applied to chemical vapor deposition (CVD)-graphene indicated a strength reduction by 40% due to grain boundaries[5]. The strength decreases with decreasing grain

[1]Institute of Mechanics, Materials and Civil Engineering, UCLouvain, Belgium. [2]Institute of Information and Communication Technologies, Electronics and Applied Mathematics, UCLouvain, Belgium. [3]School of Physics and Electronics, Hunan University, Changsha, China. [4]Laboratory for Bioinspired, Bionic, Nano, Meta Materials & Mechanics, Department of Civil, Environmental and Mechanical Engineering, University of Trento, Trento, Italy. [5]School of Engineering and Material Science, Queen Mary University of London, London, UK. [6]WEL Research Institute, Avenue Pasteur, 6, 1300 Wavre, Belgium. [7]Deceased: M. Wasil Malik. ✉e-mail: jaddi.sahar@gmail.com

boundary disorientation up to ~59%[16]. Burst testing[17] leads to a wide distribution of failure pressure, attributed to defects, slacks, and/or wrinkles in graphene. Nonetheless, applying uniaxial tension conditions on large-area crack-free graphene remains the most direct way for extracting representative strength data. Recently, in-situ push-to-pull tensile testing[17] performed on CVD-grown single-layer graphene (SLG) delivered a tensile strength of ~60 GPa with a maximum fracture strain of ~6% for ~10 μm^2 membrane. None of these methods provides fracture toughness values.

Determination of the mode I fracture toughness K_{Ic} requires going a step further with the introduction of a sharp pre-crack and a method to estimate exactly when cracking initiates. The first calculation of the fracture toughness of graphene dates back to 2004 by Pugno and Ruoff[18] reporting a value $K_{Ic} = 3.2$ or $3.45\ MPa\sqrt{m}$ for zigzag or armchair crack, respectively. Zhang et al. [19] pioneered in situ scanning electron microscope (SEM) fracture experiments on notched CVD-graphene. The specimens were mostly bilayer graphene (BLG) with a mean $K_{Ic} = 4 \pm 0.6\ MPa\sqrt{m}$. In another study, K_{Ic} of a 10-layer graphene is equal to $12 \pm 3.9\ MPa\sqrt{m}$, much higher than for SLG[20]. Cao et al.[21] followed a similar approach using push-to-pull tensile testing to study the fracture behavior of pristine BLG[22], with $K_{Ic} \approx 29.5\ MPa\sqrt{m}$. This is considerably larger than the previously reported values, and attributed to the nonlinearity of graphene[23]. The fracture of SLG was also studied by bulge testing[24], giving $K_{Ic} = 10.7 \pm 3.3\ MPa\sqrt{m}$, disclosing also the environmental cracking susceptibility of CVD-graphene. Computational studies predict $K_{Ic} = 3–4\ MPa\sqrt{m}$ by molecular dynamics simulations[9] and $K_{Ic} = 3.1 - 4.5\ MPa\sqrt{m}$ by molecular mechanics simulations[25]. The cracking process has been qualitatively investigated by transmission electron microscopy (TEM)[26,27] revealing tearing directions mostly dictated by either the zigzag or armchair directions and with limited anisotropy. All the aforementioned experimental methods are affected by the problem of introducing a sharp pre-crack, by focused ion beam damage, and by the difficulty of generating statistical data, hence not delivering foundations for a true fail-safe design.

The objective of this study is to unravel the fracture resistance of SLG by combining an original crack-on-chip (COC) and a uniaxial tension-on-chip (TOC), namely (TOCOC) experimental approach to deliver definitive statistically representative data, from which a mechanical analysis can pave the way toward fail-safe design of 2D materials-based components/devices. In an effort to overcome the shortcomings encountered in the available approaches, several challenges have been addressed in this study: (i) the specimens were tested on-chip to circumvent the gripping, clamping, and transfer problems; (ii) the specimen shape was accurately controlled through lithography methods controlled and the geometrical dimensions can be measured with precision; (iii) an on-chip loading relying on a residual stress actuation principle was adapted to avoid the use of any external macroscopic or microscopic device as well as the associated alignment issues; (iv) many samples were produced and tested simultaneously for statistical analysis; (v) different sample sizes and shapes were produced to verify if the size dependence of the fracture resistance related to the defects population can be rationalized; (vi) the crack arrest principle adopted to circumvent the artifact of a blunted starter notch instead of a true pre-crack in the fracture mechanics sense required an adapted design.

On-chip mechanical testing

The working principle of the on-chip testing method is to deform a graphene specimen by attaching it to a beam, which, when released from the substrate, contracts as a result of relaxation of internal tensile stress, thus imposing a displacement to the specimen. A schematic representation of both TOC and COC samples is shown in Fig. 1. In the

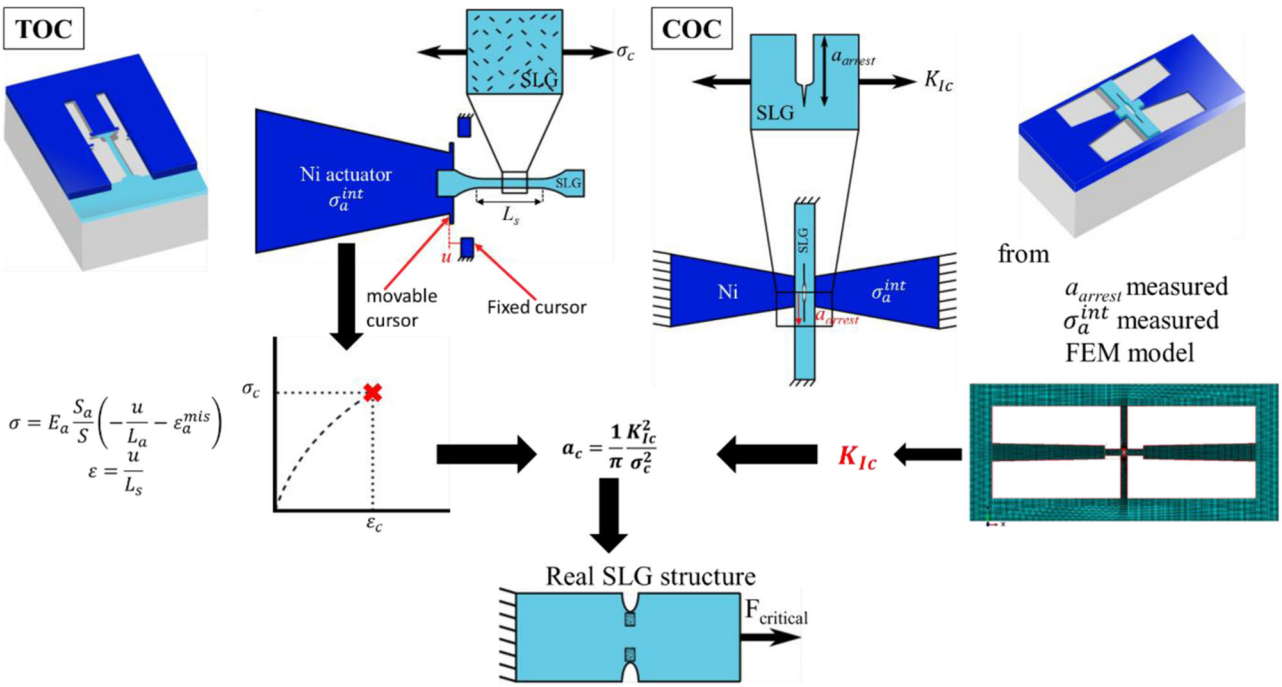

Fig. 1 | Schematic of the on-chip mechanical testing set-up applied to single-layer graphene (SLG). Both tensile-on-chip (TOC) and crack-on-chip (COC) configurations were combined to determine the critical flaw size that controls the failure of graphene membranes. The stress–strain response is given by TOC structures based on the displacement measured between movable and fixed cursors. The fracture toughness is determined using COC structures based on the measurement of the crack arrest length a_{arrest} using a finite element model (FEM). The shaded blue sample represents SLG samples with defects, a_c is the defect size that leads to fracture. The critical flaw size leading to failure a_c can be estimated once the strength and fracture toughness are known from TOC and COC, respectively. The black arrows show that to determine ac, we need to use both data coming from TOC and COC. E_a is the actuator Young's modulus, S_a is the actuator area, S is the specimen area, u is the applied displacement, L_a is the actuator length, L_s is the specimen length, ε_a^{mis} is the actuator mismatch, σ_c is the strength of the studied material, a_c is the critical flaw size, σ_a^{int} is the residual stress of the actuator prior to release and K_{Ic} is the fracture toughness.

case of the TOC configuration, the imposed displacement is generally applied to a dogbone specimen, while in the case of the COC configuration, the displacement is applied to a notched specimen to generate a crack from the tip of the notch. The working principle of the combination of the COC and TOC configurations into the new TOCOC test chain to determine the representative flaw size responsible for failure is illustrated in Fig. 1.

TOC principles have been applied to numerous thin-film systems, but never successfully adapted to 2D materials until now[14,28–33]. The specimen is deformed owing to the contraction of the attached actuator beam reaching a stable position corresponding to force equilibrium. The displacement is measured by SEM between movable and fixed cursors, as shown in Fig. 1. The internal elastic strain, also named mismatch strain in the actuator beam, is measured using dedicated structures[34,35]. The latter measurements, combined with a simple mechanical analysis[33], provide the stress-strain response (see Fig. 1 and Supplementary Note I) from which one can extract Young's modulus, strength, fracture strain, and strain hardening/softening behavior while being amenable to creep/relaxation measurements[32,36,37]. Each deformed specimen represents a single point on the stress-strain diagram. Thus, several TOC structures must be fabricated with different specimen and actuator beam lengths in order to vary the applied stress level covering the range from small elastic deformations up to fracture.

Recently, the COC concept has extended the potential of the on-chip approach, as inspired by Hatty et al.'s work[38], to extract the fracture toughness[39,40]. The core idea is that two actuator beams pull on a notched specimen. A crack initiates from the notch and then arrests (see Fig. 1). The fracture toughness is extracted from the final crack arrest length a_{arrest}, solving the problem of producing extremely sharp pre-cracks and associated artifacts, such as notch blunting effect at crack initiation. Benefiting from the lithography process to induce the pre-crack avoids the damage produced when using a focused ion beam. Finite element (FE) simulations, described in Supplementary Note II, are performed to determine K_I. Now, approximate analytical expressions have been derived as well to elucidate the effect of the different geometrical parameters and to guide the design of the test structures[39,40]. The magnitude of K_I can be roughly estimated in most cases by the following expression (see Supplementary Note III for more details):

$$K_I = (1-\nu_a)\sigma_a^{\mathrm{int}}\sqrt{L_a}\,\frac{4\sqrt{\frac{6L_a}{\alpha_2 L_s}}}{32\frac{E_a}{E}\frac{a^2}{L_s^2}+\frac{L_s}{a}\frac{L_a}{W_a}\frac{t}{t_a}}, \tag{1}$$

where ν_a is the Poisson ratio of the actuator, ν is the Poisson ratio of the test specimen (here graphene), $\alpha_2 = 1-\nu^2$ in plane strain and $\alpha_2 = 1$ in plane stress, σ_a^{int} is the residual stress in the actuator prior release, L_a is the actuator length, L_s is the specimen length, E_a is Young's modulus of the actuator, E is Young's modulus of the specimen, t_a is the actuator thickness, t is the specimen thickness, and W_a is the actuator width. The fracture toughness K_{Ic} can be estimated from Eq. (1) by using for the crack length a the final crack arrest length a_{arrest}. But, once again, FE simulations have been systematically performed to extract more accurate values for the stress intensity factor.

Equation (1) indicates that the magnitude of the stress intensity factor K_I is proportional to the residual stress in the actuator prior to release and to its length L_a, with a complex dependence on the crack length and on several other geometrical quantities. The parameters required to perform the FE simulations were determined experimentally, as given in Supplementary Table 1, with related uncertainties.

Here, we report the combined use of TOC and COC, TOCOC method, for the robust testing of 2D materials with dimensions representative of real applications, as demonstrated for monolayer CVD-graphene. In the TOCOC method, the strength of graphene σ_c obtained from TOC structures is linked to the fracture toughness K_{Ic} determined by COC structures based on $a_c = \frac{1}{\pi}\frac{K_{Ic}^2}{\sigma_c^2}$ which provides the critical defect size a_c responsible for triggering the failure of graphene-based devices, as schematically explained in Fig. 1. These structures are fabricated following the steps schematically illustrated in Supplementary Fig. 1 and explained in the "Methods" section. High-quality monolayer CVD-graphene is investigated (see the "Methods" section and Supplementary Fig. 2).

Results and discussion

Fracture toughness of monolayer CVD-graphene

Figure 2 shows a set of successful COC structures with the crack arrested at some distance from the notch for asymmetric (shown in the panel of Fig. 2a, b) and symmetric (Fig. 2d, e) configurations. Out-of-plane deflection is limited, as highlighted in the zoom of Fig. 2c. In successful test structures, the crack follows a straight path. Now, many test structures turned out to be unsuccessful for several reasons described in Supplementary Note IV. Several dies were released, leading to 80 successful COC structures (58 asymmetric and 22 symmetric).

Figure 3a compares the cumulative probability distribution of K_{Ic} for symmetric or asymmetric configurations. A majority of K_{Ic} values from both configurations are in the same range. Each structure delivers a K_{Ic} with a given uncertainty. An error propagation analysis was conducted as detailed in Supplementary Note V. The uncertainty on K_{Ic} is ~17%, coming essentially from the uncertainty on the graphene Young's modulus. The FE simulations and the uncertainty study did not take into account graphene's anisotropic elastic behavior. As a matter of fact, the elastic modulus when determined for different in-plane loading directions using the elastic constants C_{11} of 358 N/m and C_{12} of 60 N/m (from ref. 41), involves <5% variation between maximum and minimum stiffness, which is within experimental uncertainty. Considering both geometries leads to a mean fracture toughness value of $4.4 \pm 0.1\,\mathrm{MPa}\sqrt{\mathrm{m}}$, close to the $4.0 \pm 0.6\,\mathrm{MPa}\sqrt{\mathrm{m}}$ found for BLG by Zhang et al.[19], but smaller compared to multilayer graphene (MLG) data[20,22]. The standard error of $0.1\,\mathrm{MPa}\sqrt{\mathrm{m}}$ is <17% since many specimens were analyzed. The theoretical mode I fracture toughness derived from analytical calculation[18] is $3.21–3.45\,\mathrm{MPa}\sqrt{\mathrm{m}}$, and from numerical (first principle) calculations[9] is $3.9 \pm 0.4\,\mathrm{MPa}\sqrt{\mathrm{m}}$, reasonably close to our results as well.

Figure 3b compares the different experimental values reported in the literature. Note that the maximum number of tests in the literature is seven tests by Hwangbo et al.[24], much smaller than the present 80 successful tests. The reported high K_{Ic} values in the literature can be attributed to several factors. First, a multilayer can lead to toughening mechanisms due to the difference in the grain orientation in each layer and stacking order. Sliding at interfaces can also involve energy dissipation. Second, the initial crack is usually a notch and not a true precrack (~1 nm) in the sense of fracture mechanics, this is expected to nearly double the fracture toughness[42]. Third, the crack driving force can be reduced through crack branching[22,24]. The main reason behind the difference between the K_{Ic} from asymmetric or symmetric structures is attributed to the out-of-plane displacement, as confirmed by recent FE simulations performed by Shafikov et al.[43]. In addition, graphene easily buckles/crumples due to its small bending modulus and its high in-plane stiffness as demonstrated by Euler's buckling theory[44]. This twisting becomes more dominant as the length increases, thus explaining the failure of most symmetric structures as will be discussed later.

Figure 3c summarizes all the reported fracture experiments on graphene as a function of the number of graphene layers and the area of the test specimen. The graphene membrane areas tested here are around 400 and ~800 μm^2 for the asymmetric or symmetric designs, respectively, while the specimens tested in the literature do not exceed a few μm^2.

https://doi.org/10.1038/s41467-024-49426-3

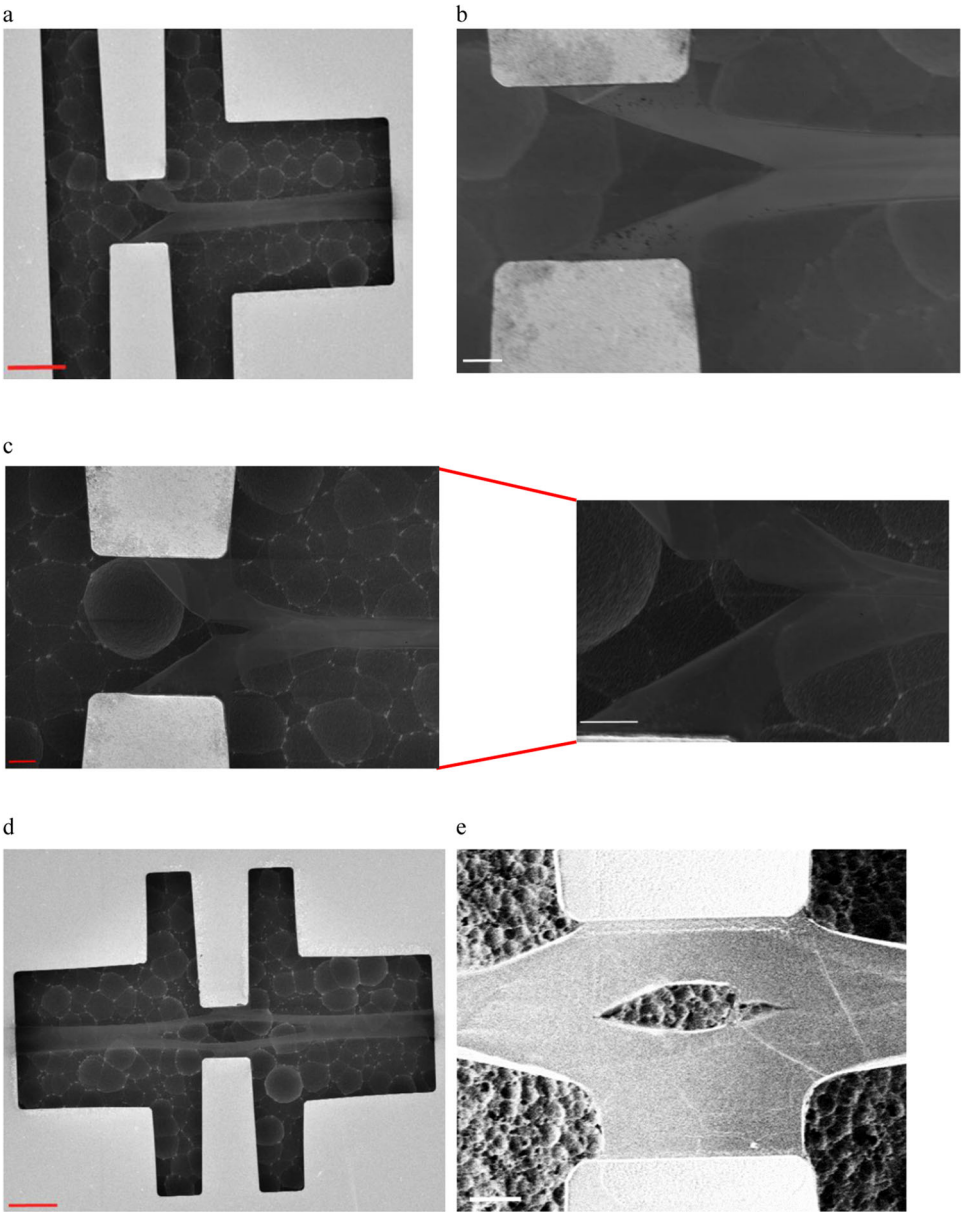

Fig. 2 | Successful monolayer CVD-graphene COC structures. a General view of an asymmetric structure in which a crack is initiated and propagated in a brittle way. **b** Closer view of an asymmetric structure shows a large crack tip opening displacement and the crack arrested after propagating over a significant distance. **c** Another asymmetric COC where the out-of-plane displacement is more evident, with a zoomed view (on the left side) showing the border between the notch and the crack. Strictly speaking, on the upper side of the notch, one can observe a kind of step marking the border between the notch and the initiated crack. **d** A general view of a successful symmetric configuration. **e** A zoomed view of the crack in a symmetric configuration where the crack opening is narrower on the left side compared with the right one- both crack lengths are close, and the cracking direction is similar. Red scale bar, 10 μm and white scale bar 2 μm.

A final point that deserves extra attention is how to explain the variations of K_{Ic} from one specimen to another within the same test configuration. First, some values at the limit of the distribution are presumably associated with specimens exhibiting wrinkles near the notch tip, which are known to accelerate failure[17], although, in other studies, wrinkles are considered as offering an extra resistance to crack propagation[24]. In any case, wrinkles artificially modify the extracted value of the fracture toughness, an effect not accounted for in our uncertainty analysis. Although the transfer was performed in such a way as to avoid producing wrinkles in graphene, the removal of the underneath layer can also introduce wrinkles in graphene[45,46]. A wrinkled freestanding graphene tends to self-fold under deformation. This is indeed what has been observed for the widest specimens, as a way to release the in-plane strain energy. In this work, the presence of wrinkles near the crack tip is unlikely, especially in all the 80 measured specimens (see Supplementary Note VI for more details). For asymmetric design, creases have been sometimes observed and can be partially responsible for the (artificial) fracture toughness variation. Another possible artifact could be due to PMMA residues on graphene. Now, the bonding strength between PMMA residues and graphene is weak besides the fact that the K_{Ic} of PMMA residues is low ~1 MPa$\sqrt{m}$[24]. Hence, PMMA residue islands can potentially affect the cracking rate and path but not the fracture toughness. Here, the cracking path was, in most cases, similar from one specimen to another excluding thus any significant impact of residues on K_{Ic}. Finally, a grain size effect on K_{Ic} is expected when the grain size is extremely small, for instance,

https://doi.org/10.1038/s41467-024-49426-3

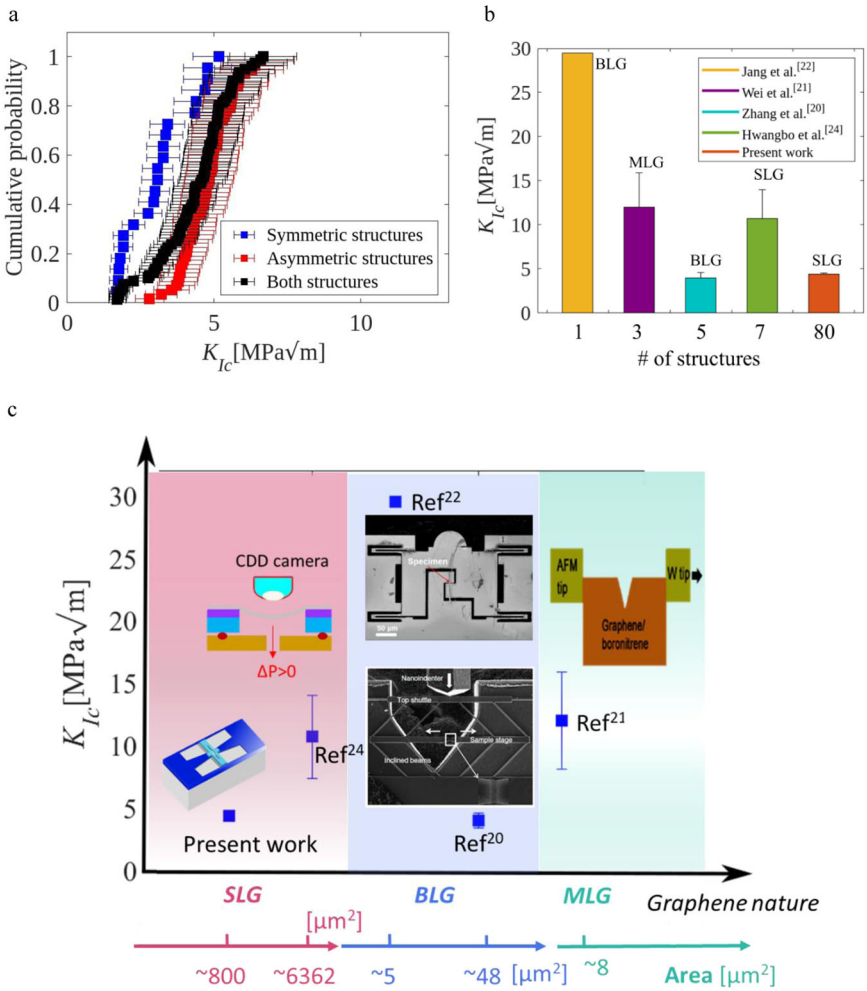

Fig. 3 | Fracture toughness of graphene, from on-chip testing and literature. **a** Fracture toughness distribution as a function of cumulative probability for symmetric structures only (in blue), for asymmetric structures only (in red), and both structures combined in black color. **b** Histograms comparing all performed experiments using graphene and the number of tests involved to determine the corresponding fracture toughness. (In addition, the nature of graphene is indicated on top of each bar. MLG is for multilayer graphene, BLG is for bilayer graphene, and SLG refers to single-layer graphene. The color code is shown in the upper right frame). **c** Comparison between the K_{Ic} measured in this study, and the reported experimental values as a function of graphene layers and specimen area—the principle of each experimental technique is illustrated by a picture. The error bar in this work is too small, which is difficult to illustrate. The error bars refer to the standard deviation. "Source data are provided as a Source Data file".

around 250 Å[9]. However, here, the interaction of the crack tip with domain/grain boundaries can also be excluded since the graphene domains in which specimens have been patterned have a size of around 3 cm (see Supplementary Fig. 3). The dispersion is thus essentially attributed to the uncertainty on the measurement of the crack length as well as on minor warping-out-of-plane effects. In conclusion, the value $K_{Ic} = 4.4 \pm 0.1\,\mathrm{MPa}\sqrt{m}$ can be safely considered as the definitive fracture toughness for monocrystalline single-layer graphene.

Strength and fracture strain of monolayer CVD-graphene

Both standard TOC dogbone (Fig. 4a) and TOC rectangular specimens (Fig. 4b) were tested (more details in the "Methods" section). The motivation behind using rectangular graphene specimens was to reduce the tendency for graphene to crumpling/tubing, as often observed in this study for the dogbone geometry. Indeed, the wider sections combined with the constraints at the clamping extremities strongly reduce the propensity for topological changes under deformation. However, the regions near the clamped regions of the rectangular sample are not undergoing perfect uniaxial tension and constitute stress concentrators. Many successful TOC structures, i.e. 222 specimens, were produced with single-layer graphene, which, per se, is an experimental accomplishment.

Figure 5a, b shows the true stress-true strain curve for single-layer graphene specimens showing no twisting, warping or crumpling, or any other observable defects. In general, narrower specimens exhibit more twisting. Therefore, the data from the widest dogbone specimens are always close to perfect homogenous uniaxial tension. Furthermore, the widest specimens offer the largest resistance to the actuator beam, leading to a smaller uncertainty on the stress determination[30]. The results shown in Fig. 5 were obtained without considering any pre-tensile stress in the graphene. By considering pre-tensile stress levels of 0.05–0.6 N m^{-1} [6,47,48], the fracture strain and stress could change by about 1%, justifying the assumption of neglecting the graphene's pre-strain. Both configurations, as detailed in the "Methods" section, lead to Young's modulus of ~950 GPa, close to the expected value (1 TPa).

The discrepancy in the TOC results can be related to the presence of wrinkles. As mentioned earlier, the quantification of the impact of wrinkles on the extracted Young's modulus is a challenging problem that has been studied numerically. Shen et al.[49] showed a negligible impact of wrinkles on the stiffness of the monolayer graphene layer. In

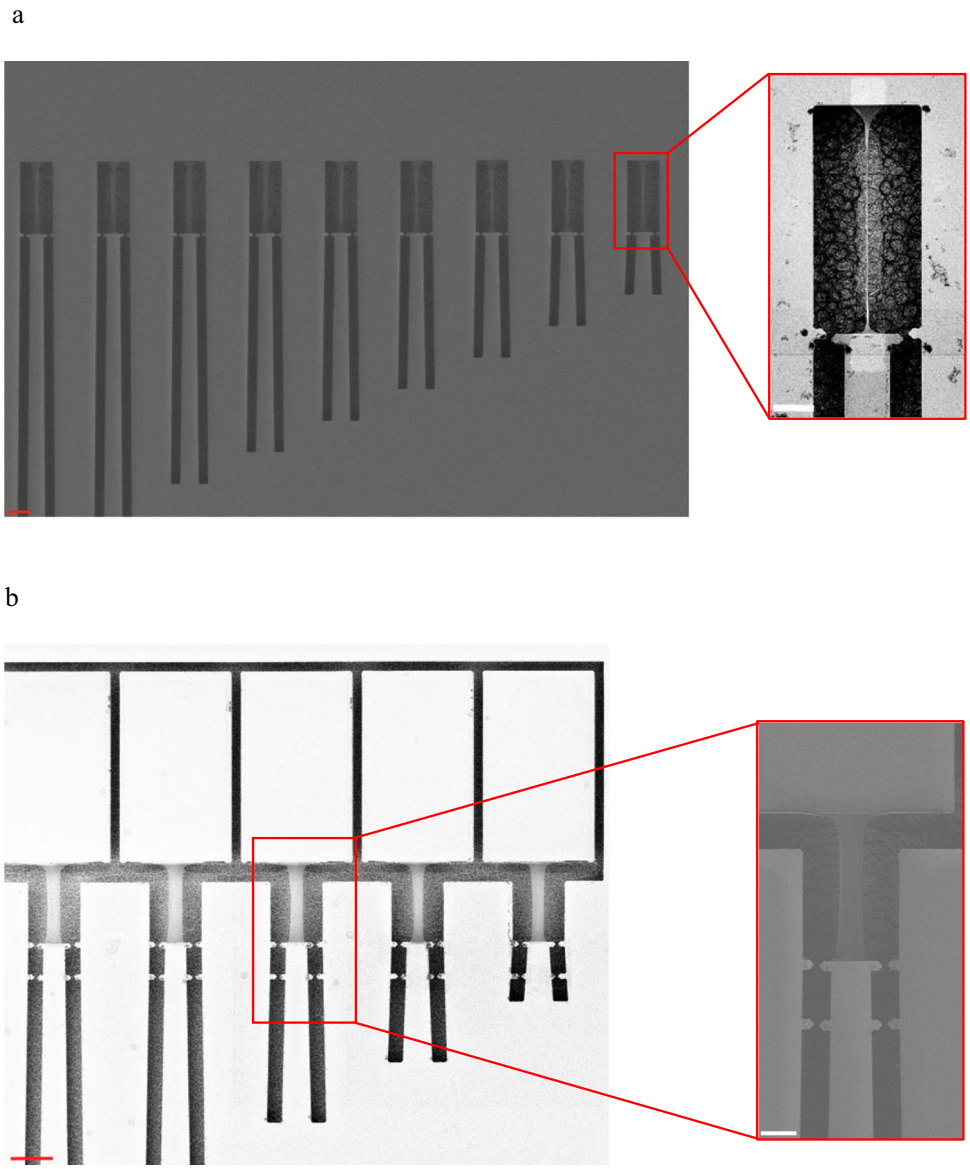

Fig. 4 | On-chip uniaxial tensile testing of graphene. a Series of 'dogbone' TOC structures with different actuator lengths. The inset is a zoomed SEM micrograph of a dogbone graphene specimen for the TOC test. **b** A series of 'Rect' TOC structures with a variety of actuator lengths. The inset is a zoomed view of a rectangular graphene specimen in the TOC configuration. The red scale bar refers to 20 μm and the white scale bar, is 10 μm.

the worst-case scenario, high wrinkle density with high wavelength involves an 11% reduction of Young's modulus along the armchair direction. About 4% reduction along a zigzag direction is in the range of the measurement error on the Young's modulus determined in this study. This value could be even lower since the wrinkle density in the present work is low. On the other hand, Qin et al.[50] reveal higher strength in the case of wrinkled graphene specimens compared with flat ones, which was used as an argument to strengthen some metal matrix composites[51]. Consequently, the extracted Young's modulus will not change drastically in the presence of a small wrinkle's amplitude. Another point worth mentioning is that the results obtained here are all consistent with one another, and when a test is repeated, even though corrugations are not uniformly distributed. This consolidates the trust in the validity of the results (more details are provided in Supplementary Note VI). Note finally that the main interest of the TOC structures was not to look at the elastic behavior but mainly to determine the fracture strain and corresponding fracture stress on a large set of specimens.

Figure 5a shows a maximum surviving strain of 0.045 with dogbone specimens, and 0.115 with rectangular ones (see Fig. 5b). This is the highest uniform deformation reached without failure in this study and, we believe, ever reported in the literature for truly uniaxial tension conditions. The maximum reported fracture strain[21] we found in the literature is ~5.8% for a ~12 μm^2 specimen area, which is half of the maximum value obtained here, and for a significantly larger specimen with a surface area equal to ~160 μm^2. The product of 1/2 × fracture stress × fracture strain = 1/2 × 110 GPa × 0.115 ≈ 6.3 GJ m^{-3} might be the largest density of mechanical energy ever stored in a freestanding material. The TOC working principle is such that the precision on the strain is much larger than on stress[30], as explained in Supplementary Note VII. Hence, the focus hereafter will be on the fracture strain, while the corresponding strength can be estimated by assuming linear elasticity and a 950 GPa Young's modulus.

Figure 5c is a plot of the deformation applied to all the test specimens as a function of the specimen length with a different symbol, whether the specimen is broken or not. Supplementary Fig. 4 shows

https://doi.org/10.1038/s41467-024-49426-3

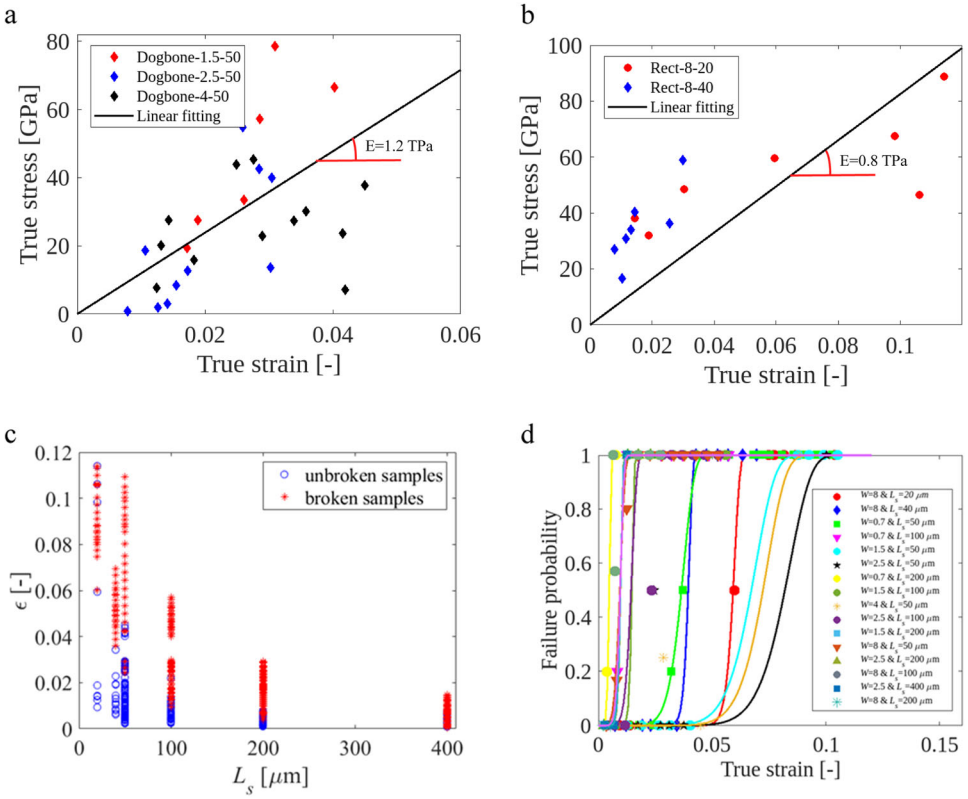

Fig. 5 | Results from TOC structures on monolayer graphene. a Uniaxial stress–strain response of single-layer graphene when considering only dogbone specimens, where 'Dogbone-*x*–*y*' refers to a specimen with a dogbone geometry, *x* μm wide and *y* μm long. **b** Stress–strain response of monolayer graphene obtained by considering only rectangular specimens, 'Rect-*x*–*y*' means rectangular sample where the first number is the width of the specimen and the second number is the specimen length. **c** Variation of the strain as a function of specimen length L_s for both broken and unbroken specimens. The strain for an unbroken specimen is the measured one. The strain corresponding to a broken specimen is the maximum strain applied to this specimen, known based on Eq. (S9). **d** Failure probability variation with true strain for different specimen lengths and widths, obtained from $N^{\varepsilon}_{\text{broken}}/(N^{\varepsilon}_{\text{broken}}+N^{\varepsilon}_{\text{unbroken}})$, where $N^{\varepsilon}_{\text{broken}}$ is the number of broken specimens undergoing a strain ε, while $N^{\varepsilon}_{\text{unbroken}}$ corresponds to unbroken specimens under strain ε. The solid line linking the data points is the fitted Weibull function, using Eq. (3). "Source data are provided as a Source Data file".

Table 1 | Parameters of the Weibull distribution

L_s [μm]	20	40	50					100				200				400
W [μm]	8.0	8.0	0.7	1.5	2.5	4.0	8.0	0.7	1.5	2.5	8.0	0.7	1.5	2.5	8.0	2.5
Weibull modulus, m	27	27	9	9	10	10	6	8	19	8	10	8	10	13	8	12
ε_0	0.06	0.040	0.038	0.070	0.085	0.075	0.01	0.01	0.015	0.015	0.005	0.005	0.01	0.01	0.01	0.01
Correlation coefficient, R^2 [%]	83	100	99.9	100	75	93	97.3	100	100	99.5	79	96.6	100	100	100	100

L_s is the specimen length and ε_0 is the characteristic strain.

the same data but as a function of the sample area. The determination of the failure probability of graphene TOC specimens is explained in the "Methods" section. Figure 5d plots the failure probability as a function of applied strain (taken as a mean value over a small interval) for different specimen lengths and widths for both rectangular and dogbone geometries, see the earlier application on aluminum films[31]. The solid lines in Fig. 5d represent the Weibull functions, with the parameters given in Table 1. The rectangular specimens are characterized by a high value of Weibull modulus $m = 27$, while the dogbone specimens exhibit a lower value of m, as detailed in Table 1. Lower m are obtained for larger specimens indicating that another population of defects/imperfections is playing a role typically due to the twisting of the specimens. Hence, one can hardly rationalize these data into one single master plot[52].

Pugno and Ruoff[53] already applied Weibull statistics at the nanoscale to carbon nanotubes, noting that point defects more than length or area/volume defects were predominant, as similarly observed here and in contrast to classical (volume-based) Weibull's statistics. In the work of Cui et al.[54], a value of $m = 13.9$ was determined experimentally under static loading, and lower values of m equal to 6.4 and 4.3 were determined under cyclic loading of 10^9 and 10^7 cycles respectively, while Shekhawat et al.[9] performed MD simulations that led to $m = 10.7$. Our values for dogbone specimens are close to the latter reported m values. The variation of m, particularly between the dogbone and rectangular graphene samples, is mainly attributed to the size and geometry differences and not to the material property since m is the same for a given material. For instance, wider samples tend to remain more in-plane compared with the longer and narrower samples that likely folded acting like nanotubes more than a flat sheet. In another vein, the variation of Weibull moduli in this work reflects the sensitivity of CVD-monolayer graphene to the presence of defects such as creases that can deteriorate under cyclic loading, as confirmed by

https://doi.org/10.1038/s41467-024-49426-3

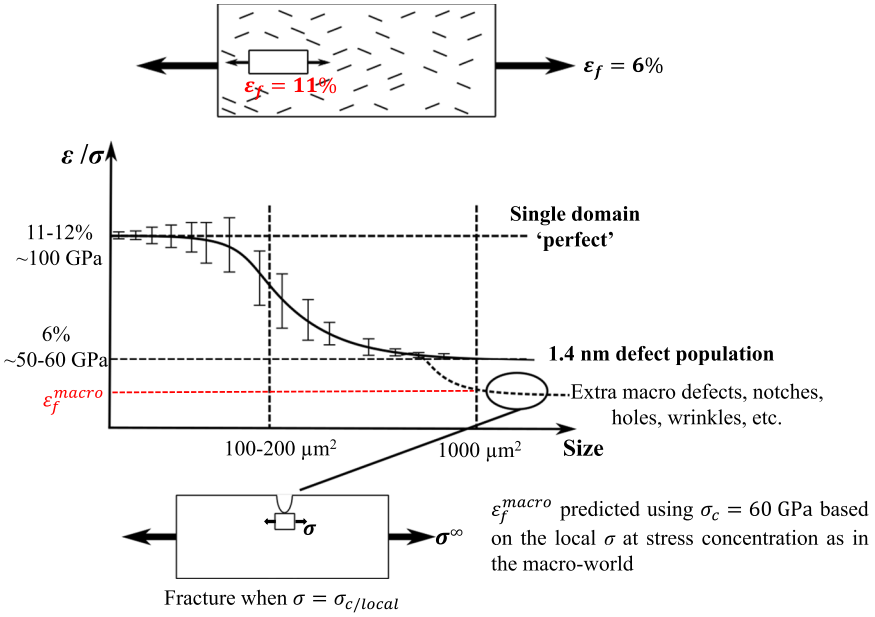

Fig. 6 | Schematic representation of how the fracture strain and strength vary as a function of the population of defects and specimen size. Extremely small specimens can sometimes be immune to any internal flaw and reach up to 11% fracture strain. Nevertheless, in general, intrinsic flaws are unavoidable for large micro-size specimens (and larger), and the fracture strain reaches the value of 6%. Lower fracture strain can be found if another population of flaws is generated or in the case of additional stress concentrators.

Cui et al.[54]. One more note, the high value of m indicates a high quality of graphene, especially for rectangular samples.

In the cleanest tensile tests performed in this work with limited "macroscopic" stress concentration and twisting, i.e. with the short L_s = 20 μm dogbone specimens, no specimen failed below 6%. The corresponding strength is equal to 57 GPa (using E = 950 GPa). Based on the fracture mechanics equation $K_{Ic} = \sigma_c\sqrt{\pi a_c}$ with σ_c the overall fracture stress and K_{Ic} = 4.4 ± 0.1 MPa$\sqrt{m}$, one can estimate the typical flaw size according to fracture mechanics, i.e. $a_c \cong 1.90$ nm. Fracture mechanics cannot predict ideal strength and cannot treat small-scale as well as not perfectly sharp defects, for this reason, quantized fracture mechanics (QFM) was introduced in Pugno and Ruoff[18]. According to QFM, the prediction of the crack size is not a_c but instead is $a_c' = a_c - b/2$ where b is the fracture quantum (for graphene it is considered to be nearly the distance between adjacent atoms, namely b = 0.25 nm, but expected to increase with the size-scale itself). For CVD graphene assuming a process temperature of 1000 or 1500 K, a thermodynamic[55] (lower bound) vacancy fraction of 5.66×10^{-36} or 3.18×10^{-24} was estimated, respectively, thus resulting in the specimens tested here (1000 μm² involves ~10^{10} atoms) in potentially defect-free structures. Assuming this scenario (a_c' = 0) for the 110 GPa specimens results in $b \cong 1.0$ nm (considering the measured fracture toughness), and, accordingly, $a_c' \cong 1.4$ nm for the ~57 GPa strength.

The fracture strain determined from modeling in the case of armchair edge[10,12,56] (~13%) is also not far from the largest experimental fracture strain from TOC specimens (~11.5%). However, the lack of studies investigating the edge effect on mechanical properties of monolayer graphene does not alter the fact that the obtained results in the case of graphene nanoribbons could be valid for graphene too. The effect of free edge warping in graphene nanoribbons was investigated numerically, revealing a decrease of Young's modulus[57] hence smaller strength, which can be valid for SLG. Thus, if the edge effect was taken into account during simulation, it probably resulted in a smaller Young's modulus, hence a smaller strength value. On a different note, the fact that larger specimens with much lower fracture strain are sometimes detected is not necessarily due to a wide distribution of flaw sizes, otherwise, also smaller specimens would fail sometimes at a strain below 6%, but to other extrinsic effects associated with experimental artifacts (specimen preparation, twisting/warping, etc.).

Accordingly, the key question that arises from these results is the origin and nature of these 1.4 nm-long defects. The most likely origin is the pentagon–heptagon pair defects. Their length, based on the work of Terdalkar et al.[11] is equal to 1.7–1.9 nm. Seemingly, the presence of these 5–7 defects as well as Stone–Thrower–Wales have been demonstrated to reduce drastically the strength and the fracture strain[58]. Under stress, a 5–7 defect leads to an elliptical cavity with a size between 1.5 and 2 nm close to the 1.4 nm defect derived in our analysis, which could act as a starter crack, as anticipated from fracture mechanics analysis.

Figure 6 shows the huge impact of 1.4 nm defects on the strength and fracture strain, especially when the specimen size increases, indicating that it is "almost impossible to fully get rid of these defects", as originally discussed in[18], except for extremely small (sub-micron) pristine specimens.

The strength is sensitive to specimen size, defects, as well as grain size. The Weibull analysis, as performed here, is the conventional approach used in the macroscopic world to design fail-safe structures and devices, which must also be used for the fail-safe design of graphene-based elements.

In summary, the mechanical properties of freestanding CVD-monolayer graphene were investigated using a new tension and crack on-chip (TOCOC) combination. The method relies on the use of tensile residual stress in an actuator beam that, once released, pulls on a notched graphene specimen to extract the fracture toughness or on a uniform tensile specimen to determine the uniaxial stress–strain response. The value K_{Ic} = 4.4 ± 0.1 MPa$\sqrt{m}$ is established as the definitive fracture toughness of single-layer graphene based on 80 successful experimental specimens. This fracture toughness value is higher than any hard thin layer in the sub-100 nm range, although still very low when compared with bulk tough steels or high entropy alloys with values above 250 MPa$\sqrt{m}$ because energy dissipation at the crack tip is limited by the thickness. The largest experimentally measured strain ever of 11.5% was determined over a large specimen area 160 μm^2. Furthermore, Young's modulus of 0.95 TPa and the

maximum strength of 110 GPa were found, close to the theoretical value and corresponding to defect-free graphene, as also confirmed by thermodynamics and quantized fracture mechanics. The mean strength is smaller than the theoretical value, being often controlled by the presence of 1.4 nm defects associated with 5–7 pairs. Such defects are most probably unavoidable with upscaled processing methods and will always lead to a maximum design strain of 5–6%, corresponding to a fracture stress of 50–60 GPa. This value should be considered as the best strength to be used for the design of graphene-based structures, except if less ideal processing leads to an additional population of larger defects, which would then result in lower strength. This simple and robust approach can be applied to other 2D materials for answering several open scientific questions related to mechanical behavior in current literature.

Methods

Fabrication process of COC and TOC

Some of the fabrication steps followed for designing graphene-based on-chip test structures differ from earlier studies on thicker films[14,28–37]. First, alignment marks are patterned, see Supplementary Fig. 1II–III, followed by the deposition of a thin gold layer as shown in Supplementary Fig. 1IV. After lift-off, the CVD-graphene is transferred onto the Si substrate (Supplementary Fig. 1V). The synthesis of graphene and transfer techniques are explained in the next subsections. Positive lithography (Supplementary Fig. 1VII) is performed to pattern the graphene specimen. PMMA is coated before depositing a positive photoresist to protect graphene (Supplementary Fig. 1VI). The unprotected parts of graphene after development are etched using oxygen plasma, and the remaining resist is removed by warm acetone (Supplementary Fig. 1VIII). The second lithography is carried out to pattern the actuator layer (Supplementary Fig. 1IX, X). This is followed by electron beam deposition of a nickel layer (Supplementary Fig. 1XI), which contains high tensile internal stress of around 600 MPa.

A 5-nm-thick Cr layer was deposited before the Ni layer to enhance the adhesion between graphene and Ni as well as between Si and Ni. The lift-off is done using hot acetone for a long duration to get rid of the resist residues (Supplementary Fig. 1XII). For TOC, one actuator beam is used, as shown in Supplementary Fig. 1XVI, while for COC, two actuator beams are designed as displayed in dark blue color in Supplementary Fig. 1XIV, XV, for asymmetric and symmetric configurations, respectively. By etching the Si substrate surface using XeF_2 (Supplementary Fig. 1XIII), the actuator beam is released from the substrate, and contracts, acting as a spring to impose a displacement on the test specimen. For the TOC method, the displacement is measured between two cursors, as highlighted in the inset of Supplementary Fig. 1XVI. While, for the COC, the measured parameter after release is the crack arrest length (Supplementary Fig. 1XV).

Graphene growth

Graphene is synthesized on copper foil (50 µm-thick, oxygen-free high conductivity, 99% purity, advent research materials) in a low-pressure chemical vapor deposition (LPCVD) system. The reactor is a horizontal hot-wall quartz tube. The gas inlet is monitored by 3 mass flow controllers connected to a pure Ar (Praxair, Research Grade, 99.9999%), an H_2/Ar (10%), and a CH_4/Ar (2000 ppm) gas bottle. The copper foil has been rinsed with diluted HCl and deionized water to eliminate possible surface contamination before being loaded into the CVD tube. The CVD tube is heated up from 22 to 1050 °C for 60 min, and the copper foil is annealed in pure Ar at a pressure of 800 mbar for 60 min. After the annealing, 20 sccm H_2/Ar is injected into the tube to remove the copper oxide on the surface of the copper foil at a pressure of 220 mbar for 10 min. 32 sccm of CH_4/Ar and 320 sccm of H_2/Ar are injected into the tube to start the growth of graphene at a pressure of 180 mbar. The CH_4/Ar and H_2/Ar ratios have been maintained during the cooling down of the tube. The separated graphene domain has been generated during the growth time of 90 min, as shown in Supplementary Fig. 5. When the growth time increases, the graphene domains merge together leading thus to a continuous graphene film. SEM and Raman's characterization confirmed that graphene is a monolayer, as shown in Supplementary Fig. 2.

Graphene transfer method

A PMMA-assisted method is used to transfer graphene. PMMA (950 PMMA A9, MircroChem) diluted in anisole (99%, Sigma-Aldrich) is directly spin-coated on graphene for one minute. PMMA has been dried in an ambient atmosphere for 24 h and the graphene on the backside of the copper foil has been etched away by Oxygen Plasma. $FeCl_3$ is used to etch the copper substrate, and the PMMA/graphene stack has been carefully rinsed with deionized water more than 5 times to remove the metallic contamination as much as possible. Then, the PMMA/graphene stack is transferred to the target substrate and dried in an ambient atmosphere for 24 h in order to remove the residue water between the graphene and the target substrate. The specimen is baked in an oven for 15 min at 150 °C. At the end, the PMMA is removed using a warm acetone bath (50 °C) for 1 h.

Description of the TOC method

Dogbone specimens have been produced with the following lengths: 50, 100, 200, and 400 µm. In addition, many widths were tested equal to 1, 1.5, 2.5, 4, and 8 µm. For rectangular specimens, a single width equal to 8 µm was used; while two different lengths were tested, equal to 20 and 40 µm. Here, the rectangular specimen will be defined as 'Rect'. The dogbone is simply noted as 'Dogbone'. The actuator length also varies to apply different levels of force, as shown in Fig. 4. This variation is between 30 and 1500 µm with a step of 30 µm for 'Rect' structures and between 50 and 1500 µm with a step of 25 µm for the 'Dogbone' configuration. The design of different specimen lengths is needed to characterize both large and small deformation regimes, using short and long specimens, respectively. These changes in specimen length, along with the different load levels allowed by varying the actuator length, are required in the case of materials exhibiting large fracture strains such as graphene.

Failure probability

The failure stress is never known exactly with the TOC method because a specimen is either broken (and one does not know exactly the strain at which it was broken) or unbroken, as there is no continuous monitoring of the specimen during the deformation process (which occurs progressively thanks to the tapering of the actuator beams until the release of the last attached point, which can be considered as a fast release). Hence, one can generate, as a function of the applied stress or strain (or as a function of a small range of applied stress or strain), a failure probability P_f by counting the number of broken specimens compared with the total number. This analysis can be repeated for different specimen sizes. The basic Weibull[15] analysis assumes that the failure probability is given by

$$P_f = 1 - exp\left[-\left(\frac{\sigma_N}{\sigma_0}\right)^m\right] \quad (2)$$

with Weibull exponent m, characteristic strength σ_0, and nominal strength σ_N. The equation is identical when expressed in terms of the applied strain ε and characteristic strain ε_0 assuming a linear elastic response. The justification of the exponential form is grounded on a weakest link model statistics, and thanks to the simplicity of the exponential functions, it satisfies the two limits, $P_f = 0$ when $\sigma_N = 0$ and $P_f \to 1$ when $\sigma_N \to +\infty$. The strength σ_0 depends on the specimen dimensions and corresponds to the stress with a probability of failure $P_f = 1 - e^{-1} = 0.63$. In the present work, the accuracy of the strain measurement is higher than the stress measurement, as explained in

Supplementary Note VII thus, using the Weibull equation as a function of the strain seems more convenient

$$P_f = 1 - exp\left[-\left(\frac{\varepsilon_N}{\varepsilon_0}\right)^m\right] \quad (3)$$

Equations (2) and (3) can be used with other reference parameters, the key information being in the Weibull exponent m.

Raman's characterization of graphene

Raman spectroscopy measurements were performed at three points (A–C), as shown in Supplementary Fig. 2a. In these three points, the 2D-band peak is sharp and narrow, as observed in Supplementary Fig. 2b. The intensity of the ratio G-band/2D-band peak is equal to 0.5, indicating that the graphene is a single layer. Moreover, graphene is of high quality since the D peak is negligible.

Data availability

Source data are provided with this paper. Any additional requests for information can be directed to, and will be fulfilled by, the corresponding authors. Source data are provided with this paper.

Code availability

The Python code used to calculate K_I at crack arrest (and thus K_{Ic}) is made available as a supplementary file.

References

1. Zhu, Y. et al. Graphene and graphene oxide: synthesis, properties, and applications. *Adv. Mater.* **22**, 3906–3924 (2010).
2. Liu, F., Ming, P. & Li, J. Ab initio calculation of ideal strength and phonon instability of graphene under tension. *Phys. Rev. B* **76**, 064120 (2007).
3. Xiao, J. R., Staniszewski, J. & Gillespie, J. W. Jr Fracture and progressive failure of defective graphene sheets and carbon nanotubes. *Compos. Struct.* **88**, 602–609 (2009).
4. Zhao, H. & Aluru, N. R. Temperature and strain-rate dependent fracture strength of graphene. *J. Appl. Phys.* **108**, 064321 (2010).
5. Lee, G. H. et al. High-strength chemical-vapor-deposited graphene and grain boundaries. *Science* **340**, 1073–1076 (2013).
6. Lee, C., Wei, X., Kysar, J. W. & Hone, J. Measurement of the elastic properties and intrinsic strength of monolayer graphene. *Science* **321**, 385–388 (2008).
7. Khare, R. et al. Coupled quantum mechanical/molecular mechanical modeling of the fracture of defective carbon nanotubes and graphene sheets. *Phys. Rev. B* **75**, 075412 (2007).
8. Zhang, T., Li, X. & Gao, H. Fracture of graphene: a review. *Int. J. Fract.* **196**, 1–31 (2015).
9. Shekhawat, A. & Ritchie, R. O. Toughness and strength of nanocrystalline graphene. *Nat. Commun.* **7**, 1–8 (2016).
10. Zhao, H., Min, K. & Aluru, N. R. Size and chirality dependent elastic properties of graphene nanoribbons under uniaxial tension. *Nano Lett.* **9**, 3012–3015 (2009).
11. Terdalkar, S. et al. Nanoscale fracture in graphene. *Chem. Phys. Lett.* **494**, 218–222 (2010).
12. Wei, Y. et al. The nature of strength enhancement and weakening by pentagon–heptagon defects in graphene. *Nat. Mater.* **11**, 759–763 (2012).
13. Dubois, S. M., Rignanese, G. M., Pardoen, T. & Charlier, J. C. Ideal strength of silicon: an ab initio study. *Phys. Rev. B* **74**, 235203 (2006).
14. Bhaskar, U. et al. On-chip tensile testing of nanoscale silicon freestanding beams. *J. Mater. Res.* **27**, 571–579 (2012).
15. Weibull, W. A statistical distribution function of wide applicability. *J. Appl. Mech.* **18**, 293–297 (1951).
16. Rasool, H. I., Ophus, C., Klug, W. S., Zettl, A. & Gimzewski, J. K. Measurement of the intrinsic strength of crystalline and polycrystalline graphene. *Nat. Commun.* **4**, 1–7 (2013).
17. Wang, L., Williams, C. M., Boutilier, M. S., Kidambi, P. R. & Karnik, R. Single-layer graphene membranes withstand ultrahigh applied pressure. *Nano Lett.* **17**, 3081–3088 (2017).
18. Pugno, N. M. & Ruoff, R. S. Quantized fracture mechanics. *Philos. Mag.* **84**, 2829–2845 (2004).
19. Zhang, P. et al. Fracture toughness of graphene. *Nat. Commun.* **5**, 1–7 (2014).
20. Wei, X. et al. Comparative fracture toughness of multilayer graphenes and boronitrenes. *Nano Lett.* **15**, 689–694 (2015).
21. Cao, K. et al. Elastic straining of free-standing monolayer graphene. *Nat. Commun.* **11**, 1–7 (2020).
22. Jang, B. et al. Uniaxial fracture test of freestanding pristine graphene using in situ tensile tester under scanning electron microscope. *Extrem. Mech. Lett.* **14**, 10–15 (2007).
23. Jang, B. et al. Asynchronous cracking with dissimilar paths in multilayer graphene. *Nanoscale* **9**, 17325–17333 (2017).
24. Hwangbo, Y. et al. Fracture characteristics of monolayer CVD-graphene. *Sci. Rep.* **4**, 1–9 (2014).
25. Jung, G., Qin, Z. & Buehler, M. J. Molecular mechanics of polycrystalline graphene with enhanced fracture toughness. *Extrem. Mech. Lett.* **2**, 52–59 (2015).
26. Meyer, J. C. et al. The structure of suspended graphene sheets. *Nature* **446**, 60–63 (2007).
27. Kim, K. et al. Ripping graphene: preferred directions. *Nano Lett.* **12**, 293–297 (2012).
28. de Boer, M. P., DelRio, F. W. & Baker, M. S. On-chip test structure suite for free-standing metal film mechanical property testing, Part I —Analysis. *Acta Mater.* **56**, 3344–3352 (2008).
29. de Boer, M. P. et al. On-chip laboratory suite for testing of free-standing metal film mechanical properties, Part II–Experiments. *Acta Mater.* **56**, 3313–3326 (2008).
30. Gravier, S. New on-chip nanomechanical testing laboratory—applications to aluminium and polysilicon thin films. *J. Microelectromech. Syst.* **18**, 555–569 (2009).
31. Coulombier, M., Boe, A., Brugger, C., Raskin, J. P. & Pardoen, T. Imperfection-sensitive ductility of aluminium thin films. *Scr. Mater.* **62**, 742–745 (2010).
32. Coulombier, M. et al. On-chip stress relaxation testing method for freestanding thin film materials. *Rev. Sci. Instrum.* **83**, 105004 (2012).
33. Ghidelli, M. et al. Homogeneous flow and size-dependent mechanical behavior in highly ductile Zr65Ni35 metallic glass films. *Acta Mater.* **131**, 246–259 (2017).
34. Boe, A., Safi, A., Coulombier, M., Pardoen, T. & Raskin, J. P. Internal stress relaxation-based method for elastic stiffness characterization of very thin films. *Thin Solid Films* **518**, 260–264 (2009).
35. Gallacher, B. J., O'Neill, A. G., Bull, S. J., Wilson, C. J. & Horsfall, A. B. Analysis of a passive sensor for predicting process-induced stress in advanced integrated circuit interconnect. *IEEE Trans. Device Mater. Reliab.* **8**, 174–181 (2008).
36. Lapouge, P. et al. A novel on-chip test method to characterize the creep behavior of metallic layers under heavy ion irradiation. *J. Nucl. Mater.* **476**, 20–29 (2016).
37. Lapouge, P. et al. Creep behavior of submicron copper films under irradiation. *Acta Mater.* **131**, 77–87 (2017).
38. Hatty, V., Kahn, H. & Heuer, A. H. Fracture toughness, fracture strength, and stress corrosion cracking of silicon dioxide thin films. *J. Microelectromech. Syst.* **17**, 943–947 (2008).
39. Jaddi, S., Coulombier, M., Raskin, J. P. & Pardoen, T. Crack on a chip test method for thin freestanding films. *J. Mech. Phys. Solids* **123**, 267–291 (2019).

40. Jaddi, S., Raskin, J. P. & Pardoen, T. On-chip environmentally assisted cracking in thin freestanding SiO_2 films. *J. Mater. Res.* **36**, 1–16 (2021).
41. Wei, X., Fragneaud, B., Marianetti, C. A. & Kysar, J. W. Nonlinear elastic behavior of graphene: ab initio calculations to continuum description. *Phys. Rev. B* **80**, 205407 (2009).
42. Pugno, N., Peng, B. & Espinosa, H. D. Predictions of strength in MEMS components with defects––a novel experimental–theoretical approach. *Int. J. Solids Struct.* **42**, 647–661 (2005).
43. Shafikov, A., van de Kruijs, R., Benschop, J., Houweling, S. & Bijkerk, F. Fracture toughness of freestanding $ZrSi_x$ thin films measured using crack-on-a-chip method. *J. Microelectromech. Syst.* **31**, 63–73 (2021).
44. Timoshenko, S. & Woinowsky-Krieger, S. *Theory of Plates and Shells* Vol. 2, 240–246 (McGraw-Hill, New York, 1959).
45. Lambin, P. Elastic properties and stability of physisorbed graphene. *Appl. Sci.* **4**, 282–304 (2014).
46. Cranford, S., Sen, D. & Buehler, M. J. Meso-origami: folding multilayer graphene sheets. *Appl. Phys. Lett.* **95**, 123121 (2009).
47. López-Polín, G. et al. Increasing the elastic modulus of graphene by controlled defect creation. *Nat. Phys.* **11**, 26–31 (2015).
48. López-Polín, G. et al. Tailoring the thermal expansion of graphene via controlled defect creation. *Carbon* **116**, 670–677 (2017).
49. Shen, X., Lin, X., Yousefi, N., Jia, J. & Kim, J. K. Wrinkling in graphene sheets and graphene oxide papers. *Carbon* **66**, 84–92 (2014).
50. Qin, H., Sun, Y., Liu, J. Z., Li, M. & Liu, Y. Negative Poisson's ratio in rippled graphene. *Nanoscale* **9**, 4135–4142 (2017).
51. Akhunova, A. K., Galiakhmetova, L. K. & Baimova, J. A. The effects of dislocation dipoles on the failure strength of wrinkled graphene from atomistic simulation. *Appl. Sci.* **13**, 9 (2022).
52. Bernal, R. A. On the application of Weibull statistics for describing strength of micro and nanostructures. *Mech. Mater.* **162**, 104057 (2021).
53. Pugno, N. M. & Ruoff, R. S. Nanoscale Weibull statistics. *J. Appl. Phys.* **99**, 024301 (2006).
54. Cui, T. et al. Fatigue of graphene. *Nat. Mater.* **19**, 405–411 (2020).
55. Pugno, N. M. Space elevator: out of order? *Nano Today* **2**, 44–47 (2007).
56. Wang, M. C., Yan, C., Ma, L., Hu, N. & Chen, M. W. Effect of defects on fracture strength of graphene sheets. *Comput. Mater. Sci.* **54**, 236–239 (2012).
57. Jiang, J. W. Strain engineering for mechanical properties in graphene nanoribbons revisited: the warping edge effect. *J. Appl. Phys.* **119**, 234301 (2016).
58. He, L., Guo, S., Lei, J., Sha, Z. & Liu, Z. The effect of Stone–Thrower–Wales defects on mechanical properties of graphene sheets—a molecular dynamics study. *Carbon* **75**, 124–132 (2014).

Acknowledgements

The authors would like to warmly thank the support of the UCLouvain WINFAB cleanroom team. This work was supported by the ARC project Naturist (Convention No. 11/16-037) and by the FNRS under Grant PDR-T.0178.19. S.J. acknowledges the support assistant mandate from UCLouvain. N.M.P. gratefully acknowledge funding by the European Comission through the GrapheneCore3 881603 Project.

Author contributions

S. Jaddi wrote and edited the original manuscript, designed and fabricated the used on-chip tensile and crack on-chip devices, carried out most of the experiments, measurements, and simulations and analyzed the results. M.W. Malik conducted graphene growth, transfer, characterization, and Raman analysis. B. Wang contributed to the graphene growth, transfer, and cleaning of the samples. N.M. Pugno contributed to data analysis and reviewing the paper. Y. Zeng supervised this work. M. Coulombier assisted in designing the samples and results discussion. J.-P. Raskin contributed to reviewing the paper, results analysis and supervising the present research. T. Pardoen wrote, reviewed the manuscript, assisted in discussing the results and supervised this research project.

Competing interests

The authors declare no competing interests.

Additional information

Supplementary information The online version contains supplementary material available at https://doi.org/10.1038/s41467-024-49426-3.

Correspondence and requests for materials should be addressed to Sahar Jaddi.

Peer review information *Nature Communications* thanks the anonymous reviewers for their contribution to the peer review of this work. A peer review file is available.

Supplementary Information

Definitive engineering strength and fracture toughness of graphene through on-chip nanomechanics

Sahar Jaddi[1], M. Wasil Malik[2†], Bin Wang[2, 3], Nicola M. Pugno[4,5], Yun Zeng[3], Michael Coulombier[1], Jean-Pierre Raskin[2], Thomas Pardoen[1]

[1]*Institute of Mechanics, Materials and Civil Engineering, UCLouvain, Belgium*
[2]*Institute of Information and Communication Technologies, Electronics and Applied Mathematics, UCLouvain, Belgium*
[3]*School of Physics and Electronics, Hunan University, China*
[4] *Laboratory for Bioinspired, Bionic, Nano, Meta Materials & Mechanics, Department of Civil, Environmental and Mechanical Engineering, University of Trento,* Trento, *Italy*[5]
School of Engineering and Material Science, Queen Mary University of London, London, United Kingdom
[6]*WEL Research Institute, avenue Pasteur, 6, 1300 Wavre, Belgium*

Supplementary Figures

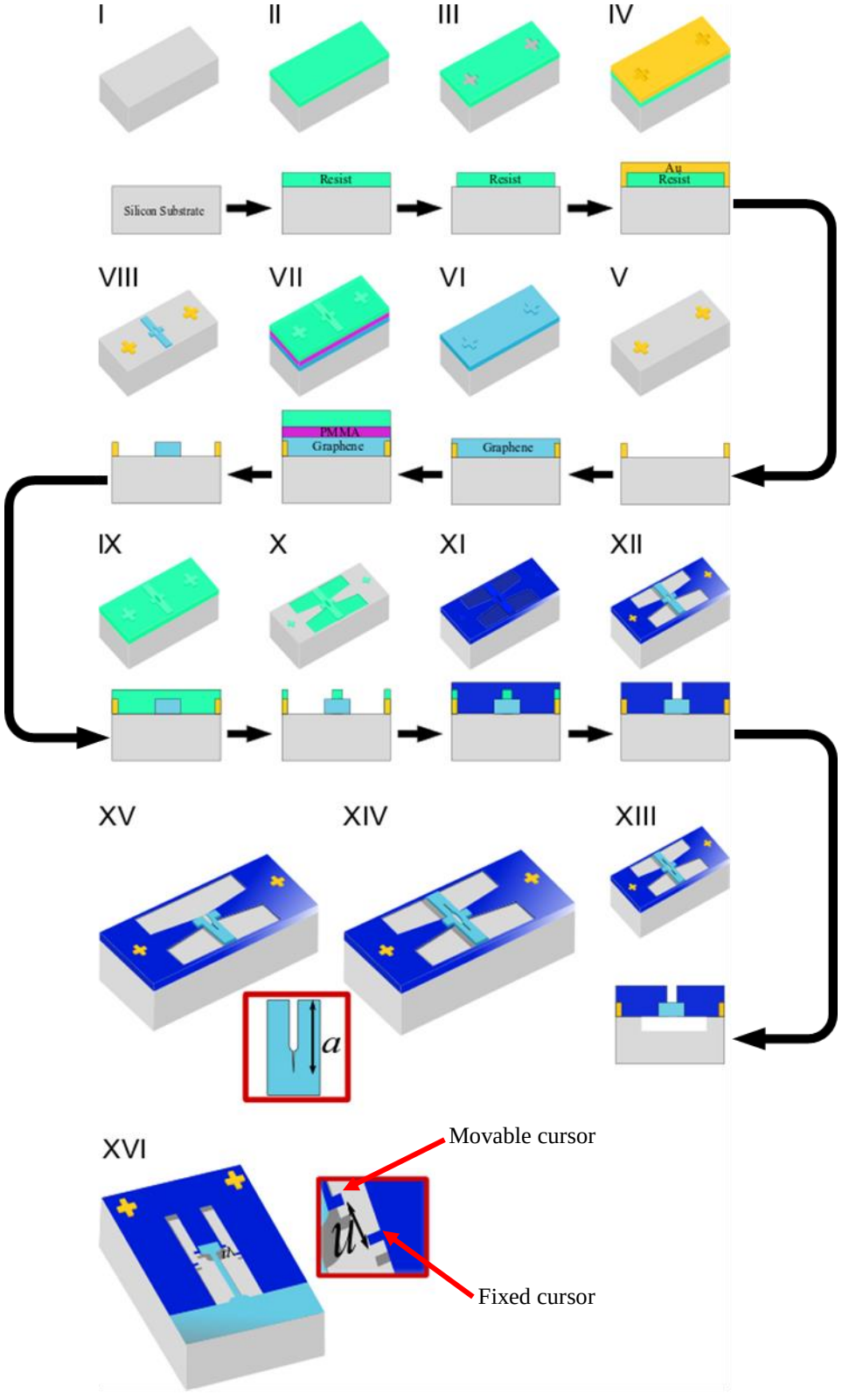

Supplementary Figure 1: I-XIII Main fabrication steps of COC and TOC applied to graphene specimens. Schematic illustration of released symmetric and asymmetric crack-on-chip COC design, respectively, in XIV and XV. The inset shows the crack arrest length measured after the release step. This length will be used to determine the fracture toughness given by each COC structure. XVI tensile-on-chip TOC design with dogbone shape specimen. The red inset is a schematic zoomed view of a TOC showing the displacement measured between two cursors after the release step, one is fixed and one is movable. The displacement *u* is used in the analytical equation to determine the strain and stress provided by the TOC structure.

(a)

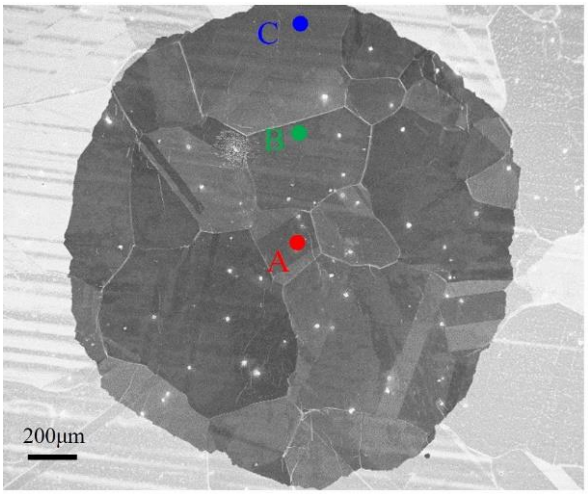

(b)

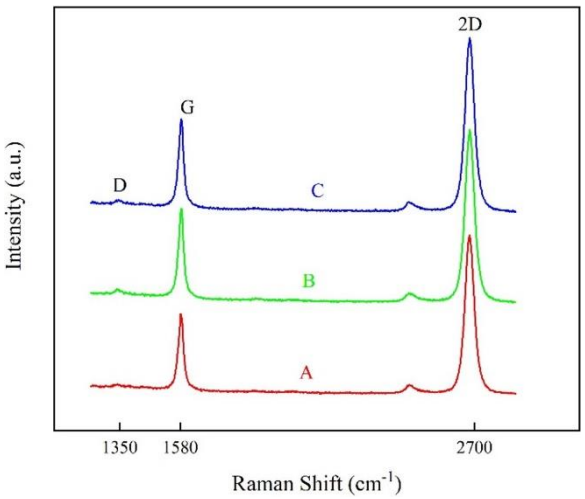

Supplementary Figure 2: Characterization of graphene domains by (a) SEM and (b) Raman (at 3 locations). G-band of around 1583 cm^{-1} is the typical value found for a flat graphene layer. The sharp 2D-band signal indicates a single-layer graphene.

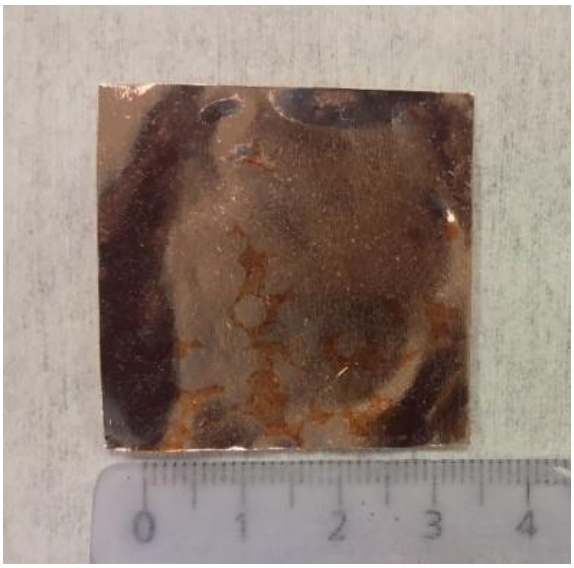

Supplementary Figure 3: The domain size of the tested CVD monolayer graphene is around 3 cm. The graphene layer covers a length of 3 cm of the Cu foil avoiding its oxidation.

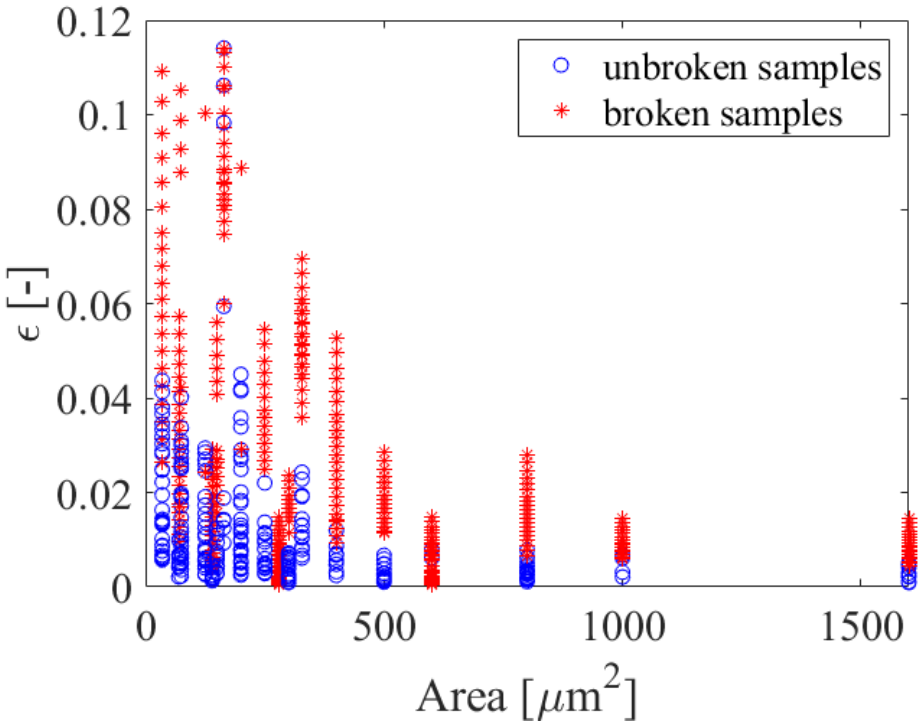

Supplementary Figure 4: TOC results of monolayer graphene as a function of the surface area of the graphene specimen. Red color for broken specimens and blue color for unbroken ones. The strain for an unbroken specimen is the measured one. The strain corresponding to a broken specimen is the maximum strain applied to this specimen, known based on equation S9.

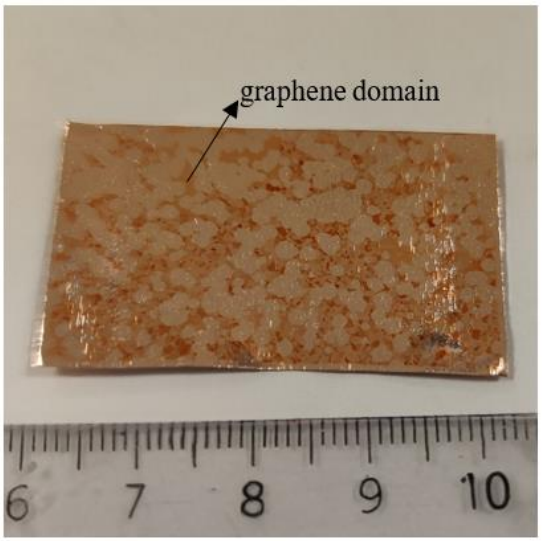

Supplementary Figure 5: Separated graphene domains on top of an oxidized Cu foil. The oxidation of copper foil occurred at the locations that were not covered by graphene (reddish zones).

Supplementary Note I: TOC mechanical model

The analytical equations describing the mechanics of the on-chip uniaxial tension test structures were developed based on linear elasticity as detailed in references [1-8]. The true stress and true strain are determined using the following relationships:

$$\varepsilon = \ln\left(\frac{L_s + u}{L_s}\right) - \varepsilon^{mis}, \tag{S1}$$

$$\sigma = A\left(\ln\left(\frac{L_a - u}{L_a}\right) - \varepsilon_a^{mis}\right)\exp(\varepsilon), \tag{S2}$$

where $A = E_a \frac{W_a t_a}{Wt}$. All parameters were determined experimentally with definition and values reported in Supplementary Table **1**. For the actuator, the mismatch strain can be determined using special test structures called self-actuated structures (shown in Supplementary Figure **6**) where the actuator beam pulls on a specimen made of the same material used as the actuator. The same technique can be used to determine the mismatch of the test specimen. However, such a test structure would not work for graphene. Alternatively, the mismatch strain can be determined using a free beam, which gives high accuracy when long enough. In practice, long free cantilevers even with a minor internal stress gradient over the thickness lead to significant out-of-plane displacement as shown in Supplementary Figure **7**. As out-of-plane displacement cannot be accurately measured, only short beams without any out-of-plane bending should be utilized, at the expense of accuracy (shorter beams involve shorter displacement upon release). In the present work, both techniques lead to a value close to the mismatch strain of the Ni actuator; $\varepsilon_a^{mis} \sim 0.003$ (self-actuated technique) and $\varepsilon_a^{mis} \sim 0.004$ (free beam). From one deposition to another, the actuator mismatch slightly changes due to several reasons related to deposition and specimen storing conditions. The latter parameter is measured in each release in order to take into account any slight variation.

Supplementary Table 1: Mechanical and geometrical parameters used in the FE simulations and uncertainties analysis for graphene specimens; E_a is Young's modulus of the actuator, E is Young's modulus of the specimen, σ_a^{int} is the internal stress of the actuator, σ^{int} is the internal stress of the specimen, ν_a is the Poisson's ratio of the actuator, ν is the Poisson's ratio of the specimen, t_a is the actuator thickness, t is specimen thickness, a is crack length, W_a is the actuator width, L_a the actuator length, L_s the specimen length, W the specimen width and W_a^s is the specimen overlap width.

Parameter	Measurement method	Value	Uncertainty
Actuator Young's modulus (E_a)	Nanoindentation	207 GPa	$\Delta E_a = 8$ GPa

Specimen Young's modulus (E)	Nanoindentation + AFM + literature[16,17]	~ 1 TPa	$\Delta E = 100$ GPa
Internal stress of the actuator (σ_a^{int})	Stoney measurement	600 MPa	$\Delta\sigma_a^{int} = 10$ MPa
Internal stress of the specimen (σ^{int})	Assumption	0 MPa	$\Delta\sigma^{int} = 10$ MPa
Poisson's ratio of the actuator (ν_a)	From literature[18]	0.3	$\Delta\nu_a$= 0.01
Poisson's ratio of the specimen (ν)	From literature[19-21]	~ 0.3	$\Delta\nu = 0.01$
Thickness of actuator (t_a)	Profilometry	70 nm	$\Delta t_a = 1$ nm
Thickness of specimen (*t*)	Raman & AFM	0.34 nm	$\Delta t = 0.02$ nm
Crack length (*a*)	SEM after release	Depending on each structure	$\Delta a = 50$ nm
Actuator width (W_a)	SEM before and after release	10.3 µm	$\Delta W_a = 50$ nm
Actuator length (L_a)	SEM (before & after)	Varies between 10 to 100 µm	$\Delta L_a = 100$ nm
Specimen length (L_s)	SEM (before & after)	6.0 - 7.7 µm	$\Delta L = 30$ nm
Specimen width (*W*)	SEM (before & after)	40 µm	$\Delta W = 30$ nm
Specimen overlap width (W_a^s)	SEM (before & after)	7.7 - 8.1 µm	$\Delta W_a^s = 30$ nm
Notch radius	SEM (before+after)	1.2 µm	$\Delta Radius = 40$ nm
Notch length	SEM (before+after)	Varies between 0 to 24 µm	$\Delta Length = 40$ nm

Released width	SEM after release using free beams (as shown in Supplementary Figure **8**)	Varies mostly between 10 to 14 µm	$\Delta L_{rel} = 500$ nm

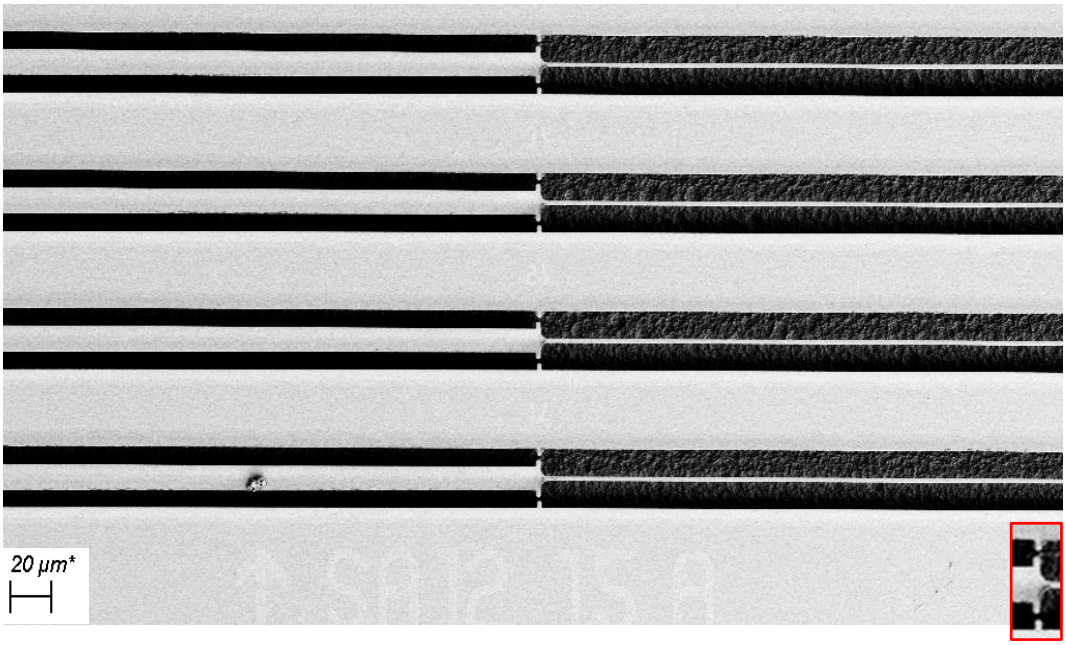

Supplementary Figure 6: SEM images of self-actuated structures of Ni films to determine the mismatch strain of the Ni actuator. Both beams are Ni films. Zoomed view of the displacement cursors in the inset.

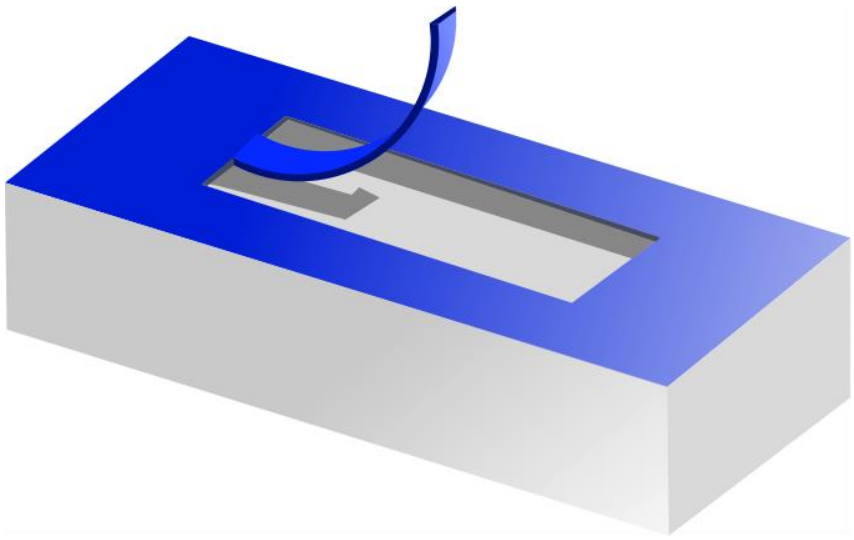

Supplementary Figure 7: Out-of-plane bending of a free actuator beam due to the internal stress gradient that is released prior to the etching of the underneath layer.

Supplementary Note II: Finite element simulation of COC

2D FE simulations have been performed using the commercial software Abaqus associated with Python scripts in order to establish an accurate data reduction scheme for the extraction of the mode I stress intensity K_I given by each structure as a function of the crack length and of the other geometrical dimensions. Details can be found in Jaddi *et al.*[9-10], and only the main aspects are summarized hereafter, in particular regarding the simulation of the release process. Furthermore, FE simulations were used to guide the design of the test structures and to analyze the kinetics of the release process.

A structure involving the test specimen, the two actuator beams, and a sufficiently wide zone of the surrounding substrate is meshed using 4-node bilinear plane stress elements with reduced integration (CPS4R). The collapsed quadrilateral quarter element technique is used to capture the singularity field near the crack tip. The overetching of the anchoring regions is taken into account as was performed in the previous study[10]. However, in this work, Ni was used as an actuator making the determination of the shape and size of the overetched zone not straightforward as opposed to the case where a transparent actuator. Thus, free beam structures (as shown in Supplementary Figure **8**) were used to determine the released area that was introduced in the simulation assuming the symmetry of the release. All nodes are initially fixed to represent the perfect adhesion to a rigid substrate. The linear isotropic elastic Hooke's law is invoked for both the specimen and actuator materials with, respectively, Poisson ratio, ν and ν_a , and Young's modulus, E and E_a.

At first, a fictitious thermal loading with the same magnitude as the measured equibiaxial internal stress was applied. Then the nodes were progressively released over time according to their shortest distance to one of the nodes located at the edges of the geometry. The node is released when the minimum calculated distance associated with a node is larger than the product of the etching rate and time. The release is stopped when the final etching time is attained, leaving several nodes at the periphery of the model unreleased, hence dictating the clamping frontier. Consequently, the value is directly provided in the form of J-integral values.

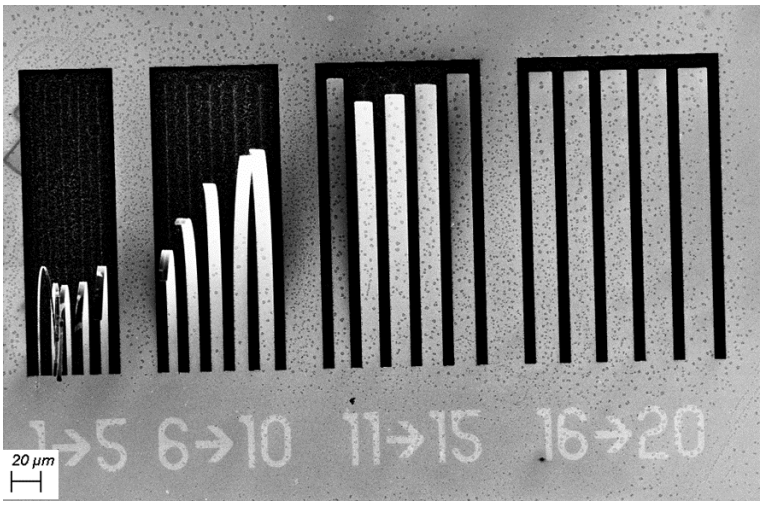

Supplementary Figure 8: SEM micrograph showing free beams with different widths used to measure the released width thus determining the overetch width. Here the 14 µm-wide beam shows out-of-plane bending which implies a 7 µm underetch. These structures are used when it is difficult to see the release profile especially when non-transparent material is used as an actuator like Ni film.

Supplementary Note III: COC principle

For short crack length *a*, the stress intensity factor can be approximately expressed by[9]

$$K_{I asym/sym} = \left(1-\nu_a\right)\sigma_a^{\text{int}}\sqrt{L_a}\,\frac{Y\sqrt{\pi\frac{a}{W}}\sqrt{\frac{W}{L_s}}\sqrt{\frac{L_a}{L_s}}}{\frac{L_a}{L_s}\frac{t}{t_a}+\frac{E_a}{2E}\left(\alpha_2 Y^2\pi\left(\frac{a}{W}\right)^2\frac{W}{L_s}+\alpha_3\right)}, \tag{S3}$$

with $Y = 1.12$ or 1 in the case of asymmetric geometry or symmetric, respectively. The two actuator beams have a length L_a, width W_a (or $2W_a$ for the symmetric design), thickness t_a, internal stress σ_a^{int}, Young's modulus E_a, and Poisson ratio ν_a. The test specimen has a length L_s, width W ($2W$ for the symmetric design), thickness t, internal stress σ^{int} that is considered equal to zero in the case of graphene, Young's modulus E, Poisson ratio ν, $\alpha_2 = 1-\nu^2$ in plane strain and $\alpha_2 = 1$ in plane stress, and $\alpha_3 = 1-\nu^2$ when the specimen is attached at its upper and lower edges and $\alpha_3 = 1$ when the specimen is free at the edges and involves a crack of length a ($2a$ for the symmetric design).

For long crack length *a*, the expression is[9]

$$K_{I\ DCB asym} = \left(1-\nu_a\right)\sigma_a^{\text{int}}\sqrt{L_a}\,\frac{4\sqrt{\frac{6L_a}{\alpha_2 L_s}}}{32\frac{E_a}{E}\frac{a^2}{L_s^2}+\frac{L_s}{a}\frac{L_a}{W_a}\frac{t}{t_a}}, \tag{S4}$$

$$K_{I\ DCB sym} = \left(1-\nu_a\right)\sigma_a^{\text{int}}\sqrt{L_a}\,\frac{4\sqrt{\frac{6L_a}{\alpha_2 L_s}}}{32\frac{E_a}{E}\frac{a^2}{L_s^2}+\frac{L_s}{a}\frac{L_a}{W_a}\frac{t}{t_a}}, \tag{S5}$$

For the graphene case, the ratio $\frac{t}{t_a}$ is almost zero. Therefore, the above equations can be simplified as for short crack length *a*:

$$K_{I asym/sym} = \left(1-\nu_a\right)\sigma_a^{\text{int}}\sqrt{L_a}\,\frac{Y\sqrt{\pi\frac{a}{W}}\sqrt{\frac{W}{L_s}}\sqrt{\frac{L_a}{L_s}}}{\frac{E_a}{2E}\left(\alpha_2 Y^2\pi\left(\frac{a}{W}\right)^2\frac{W}{L_s}+\alpha_3\right)}, \tag{S6}$$

and for long crack length *a*:

$$K_{I\,DCB\,asym/sym} = \left(1-\nu_a\right)\sigma_a^{\mathrm{int}}\sqrt{L_a}\,\frac{EL_s^2\sqrt{\dfrac{6L_a}{\alpha_2 L_s}}}{8E_a a^2}, \tag{S7}$$

Supplementary Note IV: Unsuccessful COC tests

Supplementary Figure **9** shows examples of specimen breaks before any crack initiation at the notch tip. Supplementary Figure **9**(a) shows the fracture case that often occurs in symmetric configurations and which consists of the failure of the graphene specimen in the middle part from both attached sides to both actuators or one side as shown in Supplementary Figure **9**(b). While sometimes the specimen breaks in the anchored beam from either one side or both sides as in Supplementary Figure 9(d) and (c), respectively. This fracture was driven by the fact that the two long parts of the specimen twisted due to the long length and the thinness of the graphene. Therefore, for future works, in order to be able to produce more reliable and successful symmetric structures for 2D materials, some design modifications appear necessary. A possible improvement of the symmetric design can be the large reduction of the specimen length or the addition of a new layer on top of graphene where the fracture likely occurred and far away from the cracking path. Another problem that occurred during the release is the specimen's edges twisting, especially the notch edges where the twisting can be very large as shown in Supplementary Figure **9**(e), and can transform the specimen almost into a nanotube. This problem is also associated with out-of-plane displacement and is more acute in the case of long notches. Besides the problems related to specimen design, many COC devices were not working due to many problems encountered during the fabrication process. The most common fabrication problems are the resist residues and Ni redepositing as illustrated in Supplementary Figure **9**(f).

As mentioned previously the release is performed using XeF_2 which causes fluorination if the exposure time is long introducing some defects that could affect the graphene's mechanical properties[11]. However, in our case the exposure time was very short, in total it did not exceed 40 s. Moreover, some of the samples were re-measured months after the release to check the fluorination effects since the fluorination percentage has the tendency to decrease from 50% to 80% in the week that follows the exposition[12]. Therefore, we believe that the graphene used here is not fluorinated or the fluorination effects are minuscule.

The errors generated during the crack length measurement are likely produced due to, (i) the electron charging effect that causes further cracking which is not taken into account in the extracted K_{Ic}. Although the magnification is fixed and chosen in a way to not produce further cracking, still some structures can show more charging than others; (ii) wrapping or out-of-plane bending that is more critical in graphene structures making an accurate measurement of the crack length almost impossible.

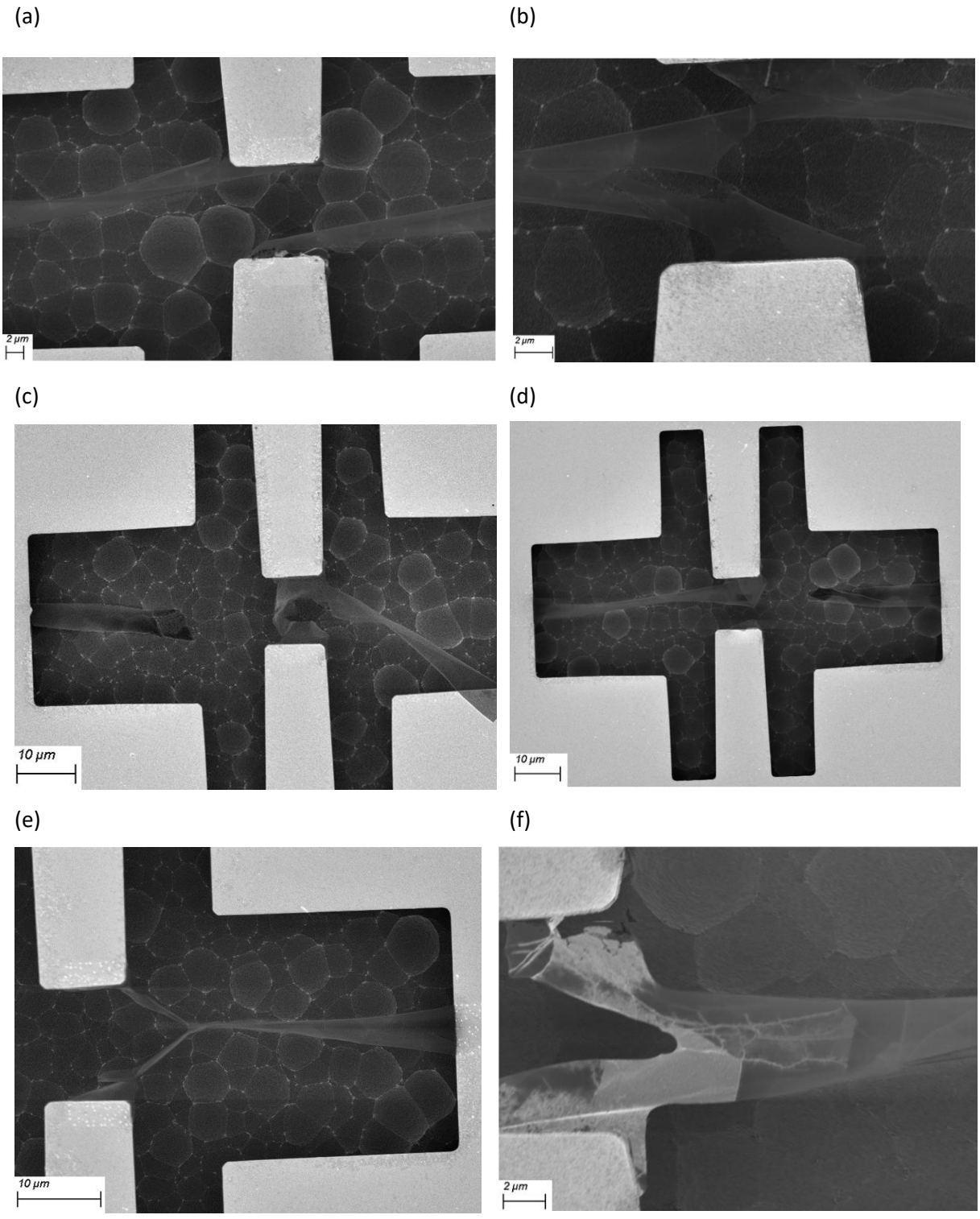

Supplementary Figure 9: Main problems encountered while testing crack-on-chip COC specimens; (a) fracture occurred in the part between the actuator on both sides, up and down; (b) fracture occurred far from the notch in the clamped beam of the graphene; (c) same as (b) but with another fracture of the other specimen's beam near the overlap between the graphene and the substrate; (d) fracture of the overlap and the specimen's beam on one side; (e) twisting of the specimen edges, precisely the notch ones; (f) resist residues and redepositing of Ni film on top of graphene membrane. The structures that undergo these problems are discarded.

Supplementary Note V: Error propagation on *K* in the case of graphene

In order to perform the error analysis, we will follow the same steps performed previously for SiO_2 in[10]. The need to redo this error propagation is necessary since here the specimen thickness is negligible and Young's modulus is very high. Therefore, the assumptions which were adopted before to simplify the analysis are no longer valid.

We rely on the analytical formula (S7). The expression includes the following independent variables: Poisson's ratio of the actuator ν_a, internal stress in the actuator σ_a^{int}, length of the actuator L_a, Young's modulus of the actuator E_a, Young's modulus of the specimen E, crack length a, the thickness of the actuator t_a, thickness of the specimen t, length of the specimen L_s, the width of the actuator W_a, $\alpha_2 = 1 - \nu^2$ where ν is the Poisson's ratio of the specimen.

We neglect the errors on W_a, t and t_a which are very small, less than 0.001%. The ratio $\frac{t}{t_a}$ tends to zero hence, the second term of the denominator is neglected in the following analysis. The formula for determining the relative error on *K* from the propagation of the different uncertainties is

$$\frac{\Delta K}{K} = \sum_i \left|\frac{\partial K}{\partial x_i}\right| \frac{\Delta x_i}{K}, \tag{S8}$$

where x_i refers to the different independent variables listed above.

The eight contributions to the overall uncertainty are derived one by one. The three first contributions from σ_a^{int}, ν_a and α_2 lead to systematic constant errors

$$\left|\frac{\partial K}{\partial \sigma_a^{int}}\right| \frac{\Delta \sigma_a^{int}}{K} = \frac{\Delta \sigma_a^{int}}{\sigma_a^{int}} = 1.67\%,$$

$$\left|\frac{\partial K}{\partial \nu_a}\right| \frac{\Delta \nu_a}{K} = \frac{\Delta \nu_a}{1 - \nu_a} = 1.4\%,$$

$$\left|\frac{\partial K}{\partial \alpha_2}\right| \frac{\Delta \alpha_2}{K} = \frac{\Delta \alpha_2}{2} = 0.55\%.$$

Since the second term of the denominator in equation (S7) is neglected, the uncertainty on *E*, E_a and on the specimen length lead to a constant contribution to the overall error:

$$\left|\frac{\partial K}{\partial E_a}\right| \frac{\Delta E_a}{K} = \frac{\Delta E_a}{E_a} = 3.86\%,$$

$$\left|\frac{\partial K}{\partial E}\right| \frac{\Delta E}{K} = \frac{\Delta E}{E} = 10\%,$$

$$\left|\frac{\partial K}{\partial L_s}\right|\frac{\Delta L_s}{K} = \frac{3}{2}\frac{\Delta L_s}{L_s} = 0.58\%.$$

The following errors vary from one structure to another:

$$\left|\frac{\partial K}{\partial L_a}\right|\frac{\Delta L_a}{K} = \frac{\Delta L_a}{L_a} < 0.9\%,$$

$$\left|\frac{\partial K}{\partial a}\right|\frac{\Delta a}{K} = \frac{2\Delta a}{a} < 3.2\%.$$

The dominant contribution is the error coming from the determination of Young's modulus of the graphene specimen.

In summary, the sum of errors is, in the best case, around 17% and can increase up to 23% in the case of short crack lengths and short actuator lengths. However, considering several specimens reduces the error on the determined mean fracture toughness.

Other phenomena might also affect the accuracy of the extracted fracture toughness that is not accounted for in the above uncertainty analysis. For instance, some values at the limit of the distribution are associated with specimens exhibiting wrinkles near the notch tip, which are known to weaken the specimen and accelerate failure[13], although, in other studies, wrinkles are considered as offering extra resistance to crack propagation[14]. In any case, wrinkles artificially modify the fracture toughness, an effect not accounted for in our uncertainty analysis. Moreover, thick graphene islands were revealed to react as crack arrestors preventing sudden crack propagation[14]. Resist residues can also act as crack arrestors and affect further the cracking rate compared with the fracture toughness. All these phenomena are described in more details in the Supplementary Material VI.

Supplementary Note VI: On the sources of imperfection/pollution in the graphene on-chip tests

In this section, the possible factors that could alter the quality of the graphene specimens are analyzed such as the presence of corrugations and PMMA residues. It also discusses how the mechanical properties are potentially influenced by the corrugations or the resist residues.

2D materials unlike their 1D or 0D counterparts exhibit corrugations such as wrinkles, ripples, creases, or crumples. These corrugations can be categorized based on their aspect ratio, order, and topology. More information regarding these corrugations has been collected in the review paper by Deng *et al*[22]. Wrinkles typically have a length longer than 100 nm, a height below 10 nm, and a high aspect ratio with widths between 1 to tens of nm. Ripples have an aspect ratio of around 1nm. Both are temporary distortions that disappear once the responsible loading conditions like compressive buckling are removed or a tensile load is applied to the sample. On the other hand, creases constitute a kind of permanent folds that are generated by applying high plastic deformation leading to a shorter sample compared with its original initial in-plane length. Last, crumples can be considered as intense wrinkles and folds occurring mostly with a 3-dimensional topology similar to a crumpled paper.

Numerous reasons lead to these corrugations in graphene such as dislocations, surface anchorage, substrate relaxation, edge or interatomic interaction instabilities, and surface tension caused by solvents. For instance, the wrinkles are known to be denser near the graphene edges and defects due to the higher asymmetric distribution of bond lengths.[23,24] Wrinkles/ripples are dependent mainly on the surface morphology of the growth substrate and on the transfer process.

Literature shows that the surface morphology underneath the graphene controls the wrinkles' density as well as their orientation.[25] Moreover, the roughness of the surface also controls the wrinkles' density since high roughness introduces extra stress to ensure adhesion between the layers leading to an increase in the number of wrinkles. Another important point is the difference in the thermal coefficient between the graphene and the underlying layer that can generate wrinkles. For instance, the epitaxy growth of graphene on top of SiC wafers shows higher wrinkles during cooling due to thermal expansion. [26,27]

In most cases, graphene is grown on top of metallic surfaces requiring to be transferred to another substrate, most likely Si, thus tending to form wrinkles. The latter can hardly be suppressed, except with very specific fine-tuned methods like the one developed by Chatterjee *et al*.[28] This transfer step could not be avoided in this study as well. Regardless of the great care taken during the graphene transfer step, we indeed still see some wrinkles in our specimens. Nevertheless, the graphene tested in this work has a low density of wrinkles thanks to the transfer method based on soaking PMMA/graphene layer in deionized water at a high temperature of around 80°C and making sure the Si surface is hydrophobic. The study conducted by Liu *et al.*[29] also by Gao *et al.*[30] shows the advantage of this transfer technique. A key point is that the area where the test structures were patterned in this work was carefully selected in a region with no or very few amount of wrinkles.

Nevertheless, the presence of wrinkles is minimized in this work especially when designing the test specimens, the etching of the underlayer also re-introduces wrinkles into graphene that becomes unstable, tending to self-folding especially with wide samples as observed in this work, and in other reported studies, e.g. in Lambin *et al.*[31] and Cranford *et al.*[32] These out-of-plane ripples/wrinkles manifest in freestanding graphene as a way to release the in-plane strain energy. The wrinkle wavelength and density increase under an applied strain especially near the edges of wide samples.

Consequently, the graphene used in this work does have some corrugations mostly in the form of wrinkles or creases. Thus, the core question is the impact of the presence of corrugations on the extracted properties. The influence of corrugations on the extracted mechanical properties is not a trivial question. It is very challenging to quantify, and up to now, to our knowledge, there is no work studying this impact experimentally in detail. To explore the potential implications, however, some research based on numerical models and theoretical calculations was carried out. According to Xi Shen *et al.*'s[33] research wrinkles have typically very little effect on the monolayer graphene sheet. For example, Young's modulus along the armchair direction is reduced by around 11% for high wrinkle density with high wavelength. The measurement error on our estimated Young's modulus, 0.85 TPa and 1.2 TPa (resulting from dogbone and rectangular samples, respectively), is in the region of 4% reduction along the zigzag direction. On the other hand, certain research, such as that by Qin *et al.*[34] demonstrated greater strength for wrinkled graphene compared to flat graphene.

Thanks to its high strength, wrinkled graphene was employed by Zhao *et al.*[35,36] to reinforce various metal matrix composites. According to Akhunova et al.'s research,[37] contrary to high-amplitude corrugations, small-amplitude corrugations in graphene do not significantly lower its Young's modulus and fracture strength. Only small-amplitude corrugations are expected to marginally lower the calculated Young's modulus and fracture strength in comparison to the pristine values. Additionally, a negative Poisson ratio was demonstrated. [34] In essence, the density of corrugations in the used samples of the present work is low and thus has a very minor impact on the extracted Young's modulus, strength, and fracture strain; this is consolidated by the repeatability of the results coming from different samples, although the non-uniformity of the corrugations distributions, and by the fact that the obtained properties values are similar to the reported values in the literature.

Regarding fracture toughness, wrinkles alter the extracted value of fracture toughness in an artificial way that is not taken into consideration by our uncertainty analysis. It is likely that some values at the limit of the distribution are related to specimens with wrinkles near the notch tip, which are known to weaken the sample and speed up failure, [38] despite the fact that in some studies wrinkles are thought to provide an additional barrier against crack propagation.[39] Nevertheless, the probability of the presence of wrinkles in the vicinity of the notch tip is negligible, especially in all the test 80 samples.

On the other hand, creases have been observed more in the asymmetric as a result of imperfections and misalignments in the geometry that can introduce significant out-of-plane displacement and can be considered somehow responsible for the discrepancy of the obtained fracture toughness values. While

the TOC (uniaxial specimens) and symmetric COC specimens do not exhibit substantial creasing upon deformation due to more constraints placed on the test structure, it is possible that the creases are encouraged by the existence of the crack. We have been running 3D FE simulations with Abaqus with imperfections, but not with the goal to generate creases and study them, but to estimate the mixed mode effects on cracking. The analysis was not pushed further because the effects were found weak. These simulations were further pursued by Twente's team who delivered convincing data. [40] The fact is that these 3D simulations never lead to creasing. This is often the case with such types of instabilities that one needs to seed the right imperfection to generate it. This appears to be a research project on its own that goes beyond what can be achieved in the context of this study.

The literature has demonstrated that PMMA-based graphene transfer results in either some form of PMMA islands or a continuous layer of residues with a thickness of 1 to 2 nm. Consequently, even in very minute amounts, PMMA residues can be found in some places of graphene. After every transfer of graphene, an SEM analysis is performed to ensure that there are no residues, at least not of a size that can be detected, in the area of interest. We are unable to offer conclusive reasoning to exclude very tiny residues. The only thing we can conclude is that the removal of PMMA residues is aided by the combination of annealing and hot acetone as was demonstrated by Hwangbo *et al.*[41] Here, the presence of a continuous film of PMMA is unlikely but we have some islands of residues with not high density thanks to using hot acetone. Hwangbo *et al.*[41] demonstrate that the bonding strength between graphene and the PMMA residues is very weak. Therefore, synergetic toughness enhancement of the graphene and residues even in the case of a uniform layer of PMMA is unlikely. In our case, the fracture toughness will not be impacted by the presence of some small/thin islands of residues, especially since the fracture toughness of PMMA is low around 1 MPa√m. However, in general, the cracking rate and path can be influenced in the case of large/thick residues that can behave as crack arrestors.

Now, assuming these minor residues would in any case be attached to certain specimens, one can reasonably expect that they would not significantly affect the mechanical behavior of graphene. This is likewise the interest of performing a large number of tests to limit the impact of some defective specimens.

As a final remark, it is worth mentioning that the step that introduces more PMMA residues is not the graphene transfer but the lithography step. This step used PMMA underneath the photoresist since residues of PMMA are easier to remove than photoresist. The removal of PMMA in this step is based on hot acetone rinses leaving a layer of resist residues. Moreover, characterizing graphene with PMMA residues is still interesting since the fabrication of graphene-based transistors and logic circuits strongly relies on PMMA as well.

As a conclusion, both PMMA residues and the different forms of corrugations can slightly change the obtained mechanical properties of the monolayer graphene.

Supplementary Note VII: When is the measured graphene displacement significantly smaller than u_{free}?

The comparison between the displacement measured when the graphene is present and with a free beam having the same length leads to a different value, which proves that although a very thin graphene layer induces a significant stress in the actuator that leads to a measurable effect on displacement. This can also be checked analytically by:

$$u = \frac{1}{1 + \frac{EWtL_{a0}}{E_a W_a t_a L_{s0}}} u_{free}. \tag{S9}$$

The second term of the denominator in equation (S9) increases when the ratio $\frac{WL_{a0}}{W_a L_{s0}}$ increases. By replacing the parameters in equation (S9) with the corresponding values. For instance, for the shortest actuator of a structure 'Rect', $u = 0.97u_{free}$, while for the longest actuator $u = 0.4u_{free}$. Therefore, for short actuator lengths, the actuator reacts like a free beam while for longer beams the difference between u and u_{free} is significant and cannot be neglected. Consequently, an approximate estimation of the stress in the monolayer graphene specimen can be determined using the TOC technique, which allows building a stress-strain response.

Supplementary References

1. Fabregue, D., Andre, N., Coulombier, M., Raskin, J. P., & Pardoen, T. Multipurpose nanomechanical testing machines revealing the size-dependent strength and high ductility of pure aluminium submicron films. *Micro & Nano Letters*, **2**, 13-16 (2007).
2. Gravier, S. et al. New on-chip nanomechanical testing laboratory-applications to aluminum and polysilicon thin films. *Journal of Microelectromechanical Systems*, **18**, 555-569 (2009).
3. Coulombier, M., Boe, A., Brugger, C., Raskin, J. P., & Pardoen, T. Imperfection-sensitive ductility of aluminium thin films. *Scripta Materialia*, **62**, 742-745 (2010).
4. Coulombier, M. et al. On-chip stress relaxation testing method for freestanding thin film materials. *Review of Scientific Instruments*, **83**, 105004 (2012).
5. Bhaskar, U. et al. On-chip tensile testing of nanoscale silicon free-standing beams. *Journal of Materials Research*, **27**, 571-579 (2012).
6. Colla, M. S. et al. Dislocation-mediated relaxation in nanograined columnar palladium films revealed by on-chip time-resolved HRTEM testing. *Nature Communications*, **6**, 1-8 (2015).

7. Vayrette, R., Raskin, J. P., & Pardoen, T. On-chip fracture testing of freestanding nanoscale materials. *Engineering Fracture Mechanics*, **150**, 222-238 (2015).
8. Ghidelli, M. et al. Homogeneous flow and size dependent mechanical behavior in highly ductile Zr65Ni35 metallic glass films. *Acta Materialia*, **131**, 246-259 (2017).
9. Jaddi, S., Coulombier, M., Raskin, J. P., and Pardoen, T. Crack on a chip test method for thin freestanding films. *Journal of the Mechanics and Physics of Solids*, **123**, 267-291 (2019).
10. Jaddi, S., Raskin, J. P., & Pardoen, T. On-chip environmentally assisted cracking in thin freestanding SiO2 films. *Journal of Materials Research*, **36**, 1-16 (2021).
11. Davami, K. *et al*. Modification of mechanical properties of vertical graphene sheets via fluorination. *RSC advances*, **6**, 11161-11166 (2016).
12. Stine, R., Lee, W. K., Whitener Jr, K. E., Robinson, J. T., and Sheehan, P. E. Chemical stability of graphene fluoride produced by exposure to XeF2. *Nano letters*, **13**, 4311-4316 (2013).
13. Wang, L., Williams, C. M., Boutilier, M. S., Kidambi, P. R., & Karnik, R. Single-layer graphene membranes withstand ultrahigh applied pressure. *Nano Letters*, **17**, 3081-3088 (2017).
14. Hwangbo, Y. et al. Fracture characteristics of monolayer CVD-graphene. *Scientific Reports*, **4**, 1-9 (2014).
15. Laconte, J. et al. Thin films stress extraction using micromachined structures and wafer curvature measurements. *Microelectronic Engineering*, **76**, 219-226 (2004).
16. Lee, C., Wei, X., Kysar, J. W., & Hone, J. Measurement of the elastic properties and intrinsic strength of monolayer graphene. *Science*, **321**, 385-388 (2008).
17. Zhang, Y., & Pan, C. Measurements of mechanical properties and number of layers of graphene from nano-indentation. *Diamond and Related Materials*, **24**, 1-5 (2012).
18. Wang, Z., Ma, Z., Zhou, Y., & Lu, C. Measurement of the mechanical properties of nickel film based on the full-field deformation: An improved blister method. *Progress in Natural Science: Materials International*, **23**, 453-458 (2013).
19. Lu, J. P. Elastic properties of carbon nanotubes and nanoropes. *Physical Review Letters*, **79**, 1297 (1997).
20. Sammalkorpi, M., Krasheninnikov, A., Kuronen, A., Nordlund, K., & Kaski, K. Mechanical properties of carbon nanotubes with vacancies and related defects. *Physical Review B*, **70**, 245416 (2004).
21. Cadelano, E., Palla, P. L., Giordano, S., & Colombo, L. Nonlinear elasticity of monolayer graphene. *Physical Review Letters*, **102**, 235502 (2009).
22. Deng, S., & Berry, V. Wrinkled, rippled and crumpled graphene: an overview of formation mechanism, electronic properties, and applications. *Materials Today*, **19**, 197-212 (2016).
23. Shenoy, V. B., Reddy, C. D., Ramasubramaniam, A., & Zhang, Y. W. Edge-stress-induced warping of graphene sheets and nanoribbons. *Physical review letters*, **101**, 245501 (2008).

24. Fasolino, A., Los, J. H., & Katsnelson, M. I. Intrinsic ripples in graphene. *Nature Materials*, **6**, 858-861 (2007).
25. Calado, V. E., Schneider, G. F., Theulings, A. M. M. G., Dekker, C., & Vandersypen, L. M. K. Formation and control of wrinkles in graphene by the wedging transfer method. *Applied Physics Letters*, **101**, (2012).
26. Vecchio, C., Sonde, S., Bongiorno, C., Rambach, M., Yakimova, R., Raineri, V., & Giannazzo, F. Nanoscale structural characterization of epitaxial graphene grown on off-axis 4H-SiC (0001). *Nanoscale Research Letters*, **6**, 1-7 (2011).
27. Biedermann, L. B., Bolen, M. L., Capano, M. A., Zemlyanov, D., & Reifenberger, R. G. Insights into few-layer epitaxial graphene growth on 4 H-SiC (000 1) substrates from STM studies. *Physical Review B*, **79**, 125411 (2009).
28. Chatterjee, S., Kim, N. Y., Pugno, N. M., Biswal, M., Cunning, B. V., Goo, M., ... & Ruoff, R. S. Synthesis of highly oriented graphite films with a low wrinkle density and near-millimeter-scale lateral grains. *Chemistry of Materials*, **32**, 3134-3143 (2020).
29. Liu, N., Pan, Z., Fu, L., Zhang, C., Dai, B., & Liu, Z. The origin of wrinkles on transferred graphene. *Nano Research*, **4**, 996-1004 (2011).
30. Gao, L., Ni, G. X., Liu, Y., Liu, B., Castro Neto, A. H., & Loh, K. P. Face-to-face transfer of wafer-scale graphene films. *Nature*, **505**, 190-194 (2014).
31. Lambin, P. Elastic properties and stability of physisorbed graphene. *Applied Sciences*, **4**, 282-304 (2014).
32. Cranford, S., Sen, D., & Buehler, M. J. Meso-origami: folding multilayer graphene sheets. *Applied physics letters*, **95**, (2009).
33. Shen, X., Jia, J., Chen, C., Li, Y., & Kim, J. K. Enhancement of mechanical properties of natural fiber composites via carbon nanotube addition. *Journal of materials science*, **49**, 3225-3233 (2014).
34. Qin, H., Sun, Y., Liu, J. Z., Li, M., & Liu, Y. Negative Poisson's ratio in rippled graphene. *Nanoscale*, **9**, 4135-4142 (2017).
35. Zhao, S., Zhang, Y., Yang, J., & Kitipornchai, S. Improving interfacial shear strength between graphene sheets by strain-induced wrinkles. *Carbon*, **168**, 135-143 (2020).
36. Zhao, S., Zhang, Y., Yang, J., & Kitipornchai, S. Folded graphene reinforced nanocomposites with superior strength and toughness: A molecular dynamics study. *Materials Science & Technology*, **120,** 196-204 (2022).
37. Akhunova, A. K., Galiakhmetova, L. K., & Baimova, J. A. The Effects of Dislocation Dipoles on the Failure Strength of Wrinkled Graphene from Atomistic Simulation. A*pplied Sciences*, **13**, 9 (2022).

38. Wang, L., Williams, C. M., Boutilier, M. S., Kidambi, P. R., & Karnik, R. Single-layer graphene membranes withstand ultrahigh applied pressure. *Nano Letters*, **17**, 3081-3088 (2017).
39. Hwangbo, Y. et al. Fracture characteristics of monolayer CVD-graphene. *Scientific Reports*, **4**, 1-9 (2014).
40. Shafikov, A., van de Kruijs, R., Benschop, J., Houweling, S., & Bijkerk, F. Fracture toughness of freestanding $ZrSi_x$ thin films measured using crack-on-a-chip method. *Journal of Microelectromechanical Systems*, **31**, 63-73 (2021).
41. Hwangbo, Y. et al. Fracture characteristics of monolayer CVD-graphene. *Scientific Reports*, **4**, 1-9 (2014).